



Fluvial and permafrost history of the lower Lena River, north-eastern Siberia, over late Quaternary time

GEORG SCHWAMBORN* , LUTZ SCHIRRMEISTER†, ALI MOHAMMADI* ,
HANNO MEYER†, ANDREI KARTOZIYA‡,§¶, FLAVIO MAGGIONI† and
JENS STRAUSS†

*Eurasia Institute of Earth Sciences, Istanbul Technical University, Maslak/Istanbul, 34469, Turkey
(E-mail: schwamborn@itu.edu.tr)

†Alfred Wegener Institute, Helmholtz Centre for Polar and Marine Research, Potsdam, 14473, Germany

‡A.A. Trofimuk Institute of Petroleum Geology and Geophysics SB RAS, Novosibirsk, 630090, Russia

§V. S. Sobolev Institute of Geology and Mineralogy SB RAS, Novosibirsk, 630090, Russia

¶Department of Geology and Geophysics, Novosibirsk State University, Novosibirsk, 630090, Russia

Associate Editor – Christopher Fielding

ABSTRACT

Arctic warming and permafrost thaw visibly expose changes in the landscape of the Lena River delta, the largest Arctic delta. Determining the past and modern river regime of thick deltaic deposits shaping the Lena River mouth in north-eastern Siberia is critical for understanding the history of delta formation and carbon sequestration. Using a 65 m long sediment core from the delta apex a set of sedimentological techniques is applied to aid in reconstructing the Lena River history. The analysis includes: (i) grain-size measurements and the determination of the bedload composition; (ii) X-ray fluorescence, X-ray diffractometry, and magnetic susceptibility measurements and heavy mineral analysis for tracking mineral change; (iii) pH, electrical conductivity, ionic concentrations, and the $\delta^{18}\text{O}$ and δD stable isotope composition from ground ice for reconstructing permafrost formation. In addition; (iv) total and dissolved organic carbon is assessed. Chronology is based on; (v) radiocarbon dating of organic material (accelerator mass spectrometry and conventional) and is complemented by two infrared – optically stimulated luminescence dates. The record stretches back approximately to Marine Isotope Stage 7. It holds periods from traction, over saltation, to suspension load sedimentation. Minerogenic signals do not indicate provenance change over time. They rather reflect the change from high energy to a lower energy regime after Last Glacial Maximum time parallel to the fining-up grain-size trend. A prominent minimum in the ground ice stable isotope record at early Holocene highlights that a river arm migration and an associated refreeze of the underlying river talik has altered the isotopic composition at that time. Fluvial re-routing might be explained by internal dynamics in the Lena River lowland or due to a tectonic movement, since the study area is placed in a zone of seismic activity. At the southern Laptev Sea margin, onshore continental compressional patterns are bordering offshore extensional normal faults.

Keywords Lena River, north-eastern Siberia, palaeoenvironment, permafrost, Quaternary.

INTRODUCTION

Growing portions of the Arctic are undergoing permafrost warming (Biskaborn *et al.*, 2019) and a prolonging of the open water season of fluvial activity is recorded for the past decades; the Lena River is one prominent example for this (Juhls *et al.*, 2020). Thawing tundra soils blanketing for example north-eastern Siberia contain about 75 times more carbon than is released by burning fossil fuels each year and twice the carbon as is presently in the atmosphere (Zimov *et al.*, 2006; Schuur *et al.*, 2008; Strauss *et al.*, 2021a). Because of the great size and volatile nature of the permafrost carbon pool (Strauss *et al.*, 2015; Jongejans *et al.*, 2021; Haugk *et al.*, 2022), decomposition of previously frozen, old organic carbon is one of the positive feedbacks to climate change in a warming world (Davidson & Janssens, 2006; Heimann & Reichstein, 2008; Strauss *et al.*, 2017; Turetsky *et al.*, 2019). Part of the ongoing effort to improve understanding of the Arctic carbon cycling is to delve into Arctic deltaic records, where great amounts of carbon have been stored and are still being deposited and released (Winterfeld *et al.*, 2015; Bröder *et al.*, 2016; Martens *et al.*, 2020). Arctic riverine fluxes are anticipated to increase as the Arctic warms. Carbon-rich deltas receive growing attention because they are dynamic interfaces of land–ocean interaction (Piliouras & Rowland, 2020).

A dynamic environment of storage and release of organic-rich deposits is the Lena River delta, which is the largest delta in the Arctic occupying 32 000 km²; it has been recognized for its complex geomorphic environments caused by neotectonic block movements (Are & Reimnitz, 2000; Schwamborn *et al.*, 2002). They control the formation of an island archipelago with elevation differences as large as 60 m, which are related to distinct geological units. The active delta occupies spaces between older islands of the archipelago and is just beginning to protrude into the open sea, especially in the eastern half (Fig. 1A and B). The Lena River is the main sediment source for the Laptev Sea, where annual drift ice distributes material as far as into the central Arctic Ocean (Peregovich *et al.*, 1999). Estimates give the suspended sediment load in the lower Lena River at 21 Mt year⁻¹ with <30% of this load thought to reach the sea (Are & Reimnitz, 2000). Fedorova *et al.* (2015, and references therein) cite measurements saying that the amount of bottom sediments is about 5.4 Mt year⁻¹ and Fofonova *et al.* (2018,

references therein) cite measurements saying that the annual bedload flux has been measured to be 14.9 Mt year⁻¹ at Kyusur gauging station, which lies 200 km south of the Lena River delta. Exploration of deltaic sediment records allow to investigate the conditions of sediment deposition with biogeochemical and palaeoenvironmental archives (Schwamborn *et al.*, 2002; Schirrmeister *et al.*, 2003, 2011; Wetterich *et al.*, 2008, 2020, 2021). However, much of the observation has been restricted to exposures and to shallow coring down to 10 m depth with floodplain deposits being the dominant sediment type (Bolshiyarov *et al.*, 2015).

This study focuses on a 65 m long permafrost core (namely: SAM18-01) that has been retrieved in 2018 (Jongejans *et al.*, 2019) from near the delta apex on Samoylov Island (72°22′37″N, 126°28′51″E, Fig. 1B and C). Using a multiple set of sediment and ground ice data, the cryosedimentary record is explored back in time and adds onto existing models of Lena River history and delta growth (Fig. 1D).

METHODS

Field work and core preparation

Core SAM18-01 was drilled using a Russian URB2-4T drilling rig (Jongejans *et al.*, 2019), which has two hydraulic cylinders that control the rotating drill rods and the core barrel. Down to 5 m borehole depth a 146 mm drilling head diameter, between 5 m and 50 m a 127 mm drilling head diameter, and between 50 m and 65 m depth a 108 mm drilling head was used. Once frozen core segments were retrieved to the surface, they were pushed-out with pressured air, described and photographically documented. Each frozen segment has been cut vertically already in the field using an angle grinder in a freezing laboratory at MPI-Yakutsk. Later in the cold laboratory at AWI-Potsdam, core segments have been cleaned, and the description and photographic documentation has been completed. The core was cryolithologically described according to French & Shur (2010). Samples have been taken at regular intervals averaging one sample per metre (70 samples in total) and according to sediment change.

Sample processing

Frozen samples were allowed to thaw and settle, and samples have been weighed. Excess water

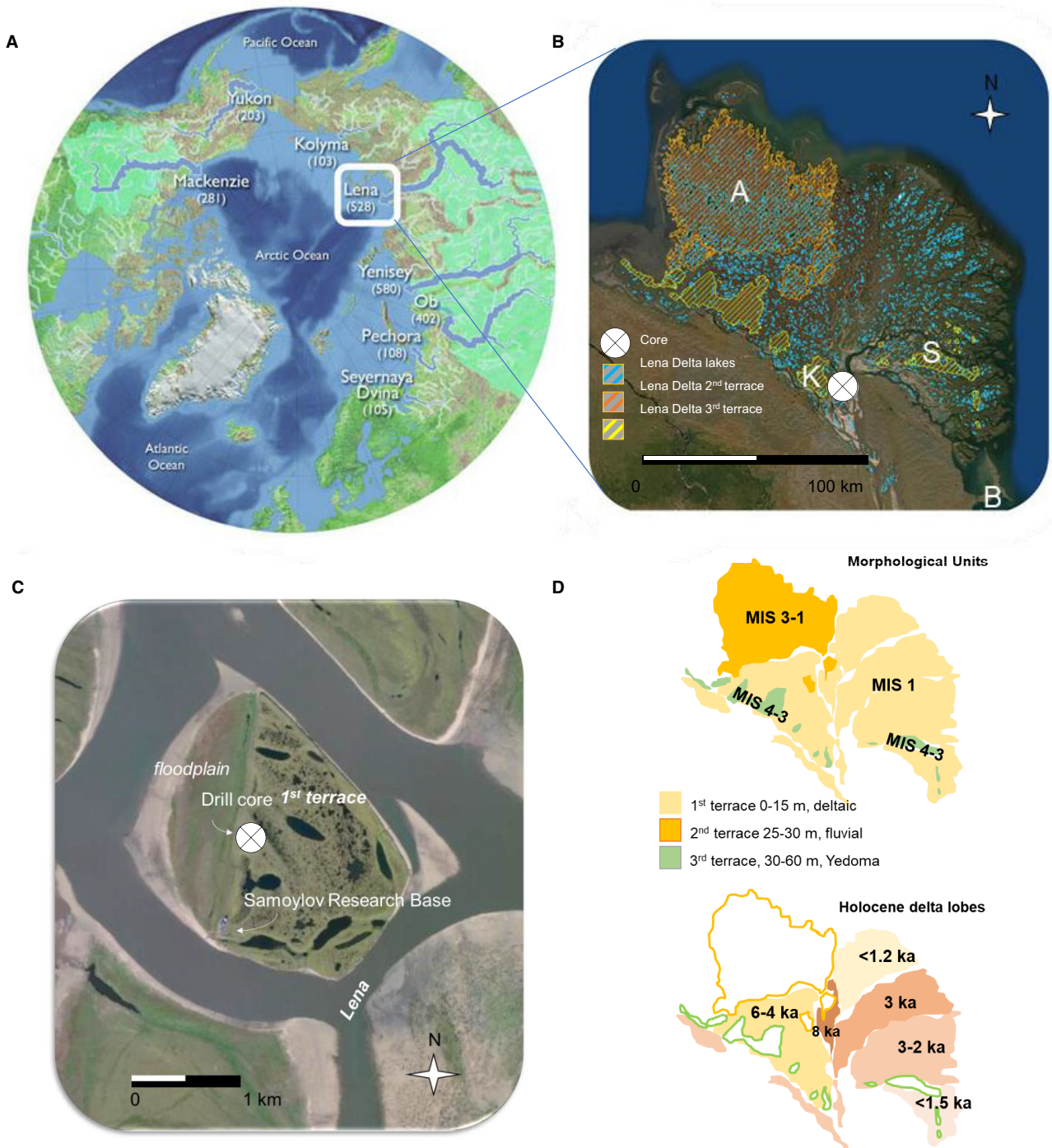


Fig. 1. Study area and coring site. (A) The Lena River (white box) has highest river discharge in the Arctic (numbers on the map are in $\text{km}^3 \text{a}^{-1}$, modified from ACIA, 2004). (B) Borehole SAM18-01 is located near the Lena River delta apex (Basemap: ESRI). Letters point to other study sites mentioned in the text; A = Arga Island, B = Bykovsky Peninsula, K = Kurungnakh Island, S = Sobo Island. (C) The coring site is placed on Samoylov Island, which is part of the first terrace (Basemap: ESRI). (D) Display of age distributions of Lena Delta geomorphological units and delta lobes according to previous studies (modified from Schwamborn *et al.*, 2002 and Bolshiyarov *et al.*, 2015).

has been sampled for hydrochemical properties [i.e. pH, electrical conductivity (EC), dissolved organic carbon (DOC) and ground ice stable isotopes $\delta^{18}\text{O}$, δD]. Remaining sample material has been freeze-dried and re-weighed for retrieving the gravimetric ice content. Subsamples from the fraction <2 mm have been milled for further analysis; i.e. X-ray fluorescence (XRF) and X-ray diffractometry (XRD), and total organic carbon (TOC) and total nitrogen (N).

Chronostratigraphy

The chronology is derived from accelerator mass spectrometry (AMS) radiocarbon dating of organic material using a MICADAS facility (MIni radioCARbon DAting System, AWI Bremerhaven, Mollenhauer *et al.*, 2021) and conventional facilities at KÖPPEN-Laboratory (a Perkin Elmer Quantulus 1220 liquid scintillation spectrometer at Saint Petersburg State University; Perkin Elmer, Waltham, MA, USA). ^{14}C AMS ages have been calibrated into calendar years according to Stuiver & Reimer (1993) which is implemented into the CALIB web tool (calib.org; version 8.20, 2021). In addition, two infrared – optically stimulated luminescence (IR-OSL) ages are available from the lower core part (Bolshiyarov *et al.*, 2020). These samples were dated by the Research Laboratory for Quaternary Geochronology (RLQG) of the Institute of Geology in the Tallinn University of Technology (Molodkov, 2020). For the sake of care these ages are treated with caution, since no additional information on bleaching or inheriting effects or laboratory protocol details are reported in Bolshiyarov *et al.* (2020).

Bulk sediment analyses

The mass specific magnetic susceptibility has been measured from subsamples of the fraction <2 mm using a Bartington MS2 Magnetic Susceptibility System (Bartington Instruments Limited, Witney, UK) using the low frequency option (e.g. Lecoanet *et al.*, 1999). The data are expressed in SI units (i.e. $10^{-8} \text{ m}^3 \text{ kg}^{-1}$) and are normalized to 10 g net weight. Mass-specific magnetic susceptibility is controlled by the content of ferromagnetic and paramagnetic minerals in the sediment (i.e. magnetite, spinel and haematite; Butler & Butler, 1992).

The bulk mineral composition of freeze-dried and milled samples has been analysed using a Rigaku Miniflex XRD (Rigaku Corporation,

Tokyo, Japan) using Ni-filtered Cu $K\alpha$ at 15 kV – 40 mA instrumental settings. Data evaluation is based on intensity peak values and their ratios for tracking relative quantities of the following phases; Quartz (4.26 Å), Orthoclase (3.24 Å) and Plagioclase (3.18 Å), Pyroxene (3 Å + 2.92 Å), Amphibole (8.4 Å), Smectite (15 Å), Illite (10 Å) and Kaolinite+Chlorite (7.1 Å). Accuracy of this semi-quantitative XRD method is estimated to be between 5% and 10% (Gingele *et al.*, 2001).

Complementary bulk geochemical composition has been measured using an ITRAX core scanner equipped with a Mo X-ray tube source for determining semi-quantitatively element composition at sample resolution (Cox Analytical Systems, Mölndal, Sweden). The X-ray generator was operated at 30 kV and 50 mA, and each sample was measured seven to eight times when moving the sample in 2.5 mm steps across focus. The relative elemental abundances were recorded as counts per second (cps) and a mean from all iterative measurements was calculated for each sample. XRF elemental detection is robust for a spectrum of medium-heavy and lighter elements; i.e. Si, Al, S, Cl, K, Ca, Ti, Fe, As, Pb, Zn, Br, Rb, Sr, Zr and Ba following Croudace *et al.* (2006).

Total organic carbon (TOC) content was measured on a VarioMax C (Elementar Analysensysteme GmbH, Langenselbold, Germany) based on the amount of CO_2 released by total catalytic combustion at 400°C and inferred from heat conductivity. Instrumental precision was monitored using reference samples with known substrate mixtures of different ratios (EDTA 5:45 4.11%, CaCO_3 6%, CaCO_3 12%, IVA 2176 15.57%). The detection limit is set at 0.1 wt%. Total nitrogen (TN) was measured on a rapid MAX N based on total catalytic combustion at 750°C and also inferred from heat conductivity. Instrumental precision was monitored using reference samples with known substrate mixtures of different ratios (bs2 0.064%, bs1 0.216%, IVA 2150 0.490%, EDTA 10:40 1.918%). The detection limit is set at 0.1 wt%.

Samples for $\delta^{13}\text{C}$ analyses were treated with hydrochloric acid (20 ml, 1.3 molar, 50°C for 3 h) to remove inorganic carbon and washed with distilled water. All $\delta^{13}\text{C}$ samples were measured using a Delta V Advantage isotope ratio MS equipped with a Flash 2000 Analyser (ThermoFisher Scientific, Waltham, MA, USA), using helium as a carrier gas. The $\delta^{13}\text{C}$ ($^{13}\text{C}/^{12}\text{C}$) value is reported in permil (‰) compared to the standard ratio of the Vienna Pee Dee Belemnite

(VPDB). External standards were used to control the instrument precision and the range of replicate stable carbon isotope measurements was generally less than $\pm 0.15\%$.

Grain-size composition

Sediment grain-size distributions are derived from sieves (fractions >2 mm) and a laser diffraction grain-size analyser (fractions <2 mm). Prior to laser sizing (Malvern Mastersizer 3000; Malvern Panalytical, Malvern, UK), the individual samples were oxidized ($3\% \text{H}_2\text{O}_2$) on a platform shaker to remove organic matter, and dispersed ($10\% \text{NH}_4\text{OH}$) to diminish the surface tension. Grain-size data are sorted to phi fractions using GRADISTAT v 9.1, a grain-size distribution and statistics package for the analysis of unconsolidated sediments by sieving or laser granulometer (Blott & Pye, 2001). This study does not account for discrepancies between the two techniques (particle sieving = wt%; particle sizing = vol%). All phi fractions are constrained to a closed-sum of 100% per sample.

Heavy mineral composition

Heavy mineral analysis has been applied to the 63 to 125 μm sieved subfraction. The heavy minerals were separated using a sodium metatungstate solution ($\text{Na}_6(\text{H}_2\text{W}_{12}\text{O}_{40}) \cdot \text{H}_2\text{O}$) with a density of 2.89 g cm^{-3} in a centrifuge. For inspection under a petrographic microscope the heavy minerals have been mounted between a glass slab and a cover using Melmount 1.68TM (Cargille Laboratories, Cedar Grove, NJ, USA). Around 200 grains were counted by applying the mid-point ribbon and fleet counting methods following standard procedures as outlined in Mange & Maurer (2012). In addition, rock fragments have been studied, as obtained from the 2.0 to 3.15 mm sieved subfraction (phi -1 to -2). Nine thin sections were produced from rock fragments embedded in epoxy resin and rock type identification has been completed using polarizing microscopy.

Hydrochemistry and stable water isotopes ($\delta^{18}\text{O}$, δD)

Ground ice content has been measured as water content in weight percent (wt%) after thaw. Analysis of pH and electrical conductivity (EC) from thawed ground ice has been done using WTW probes Sentix 81 for measuring pH and a Tetra-Con 325 for measuring EC. The anions (Cl^- ,

SO_4^{2-}) were assessed using ion chromatography (Dionex DX-320; Thermo Fisher Scientific) and concentrations are expressed as mg l^{-1} .

DOC (dissolved organic carbon) concentrations were analysed using high temperature catalytic oxidation (TOC-VCPH, Shimadzu, Kyoto, Japan). Four replicate measurements of each sample were averaged. Repeatedly a blank (Milli-Q water) and a standard were measured. Six different certified standards cover a range between 0.49 mg l^{-1} (DWNSVW-15) and 105 mg l^{-1} (IQC103), and the instrumental accuracy in terms of reproducing these standards was better than $\pm 5\%$.

Stable water isotopic composition ($\delta^{18}\text{O}$, δD) has been measured on a Finnigan MAT Delta-S mass spectrometer at the AWI Potsdam ISOLAB stable isotope facility. The values are given in delta notation (δ) as per mil (‰) difference from the Vienna Standard Mean Ocean Water (VSMOW) standard. Internal 1σ errors are better than 0.8% for δD and 0.1% for $\delta^{18}\text{O}$ following Meyer *et al.* (2000). The deuterium excess (*d-excess*) has been calculated according to Dansgaard (1964) as $d = \delta\text{D} - 8\delta^{18}\text{O}$.

Statistical treatment

The bulk mineralogical (XRF and XRD) and grain-size data are of compositional nature, which means that they are vectors of non-negative values subjected to a closed-sum constraint (usually 100%). This implies that relevant information is contained in the relative magnitudes and elemental and mineralogical data analyses can focus on the ratios between components (Aitchison, 1990). Prior to PCA (principal component analysis) and k-means cluster analyses, a centred-log ratio transformation has been applied to the compositional data sets following Aitchison (1990). The PAST software package (version Past 4.05, 2021) supported statistical calculations (Hammer *et al.*, 2001).

RESULTS

Cryostratigraphy

Three main sediment units can be distinguished; a pebbly unit at the bottom core part between 65 m and 45 m core depth with rounded, subrounded, to subangular clasts that can measure up to 4 cm. Layers between 65.9 m and 64.9 m core depth are rich in pebbles, and very coarse

pebble scatters in layers up to 46 m core depth. A sandy middle core part measures from 45 to 25 m core depth, and the top core part measures from 25 m to the surface and is dominated by organic-rich silt dominated layers (Fig. 2). Sandy layers are intercalated into this unit (see Schwamborn *et al.*, 2022).

Organic detritus in the form of individual plant fragments and drift wood pieces is admixed with sediments from mid core between 49.6 m and 27 m core depth; i.e. it is scattered at 49 m and 44 m core depth, and fragments of

drift wood appear at 37.85 m, 35.90 m, 35.10 m and 28.40 m depth. At similar core depths peaty intercalations are observed in the record; i.e. at 36 m and at 34 m core depth. Between 25 m core depth and the surface, organic detritus is a common component in much of the sandy to silty sediment. Exceptional peat layers stick out at 23.00 to 22.30 m and between 9.0 m and 5.15 m core depth.

The core holds ground ice mostly as pore ice. Some exceptions occur, when ice is segregated (Fig. 2). The bottom core part between 65 m and

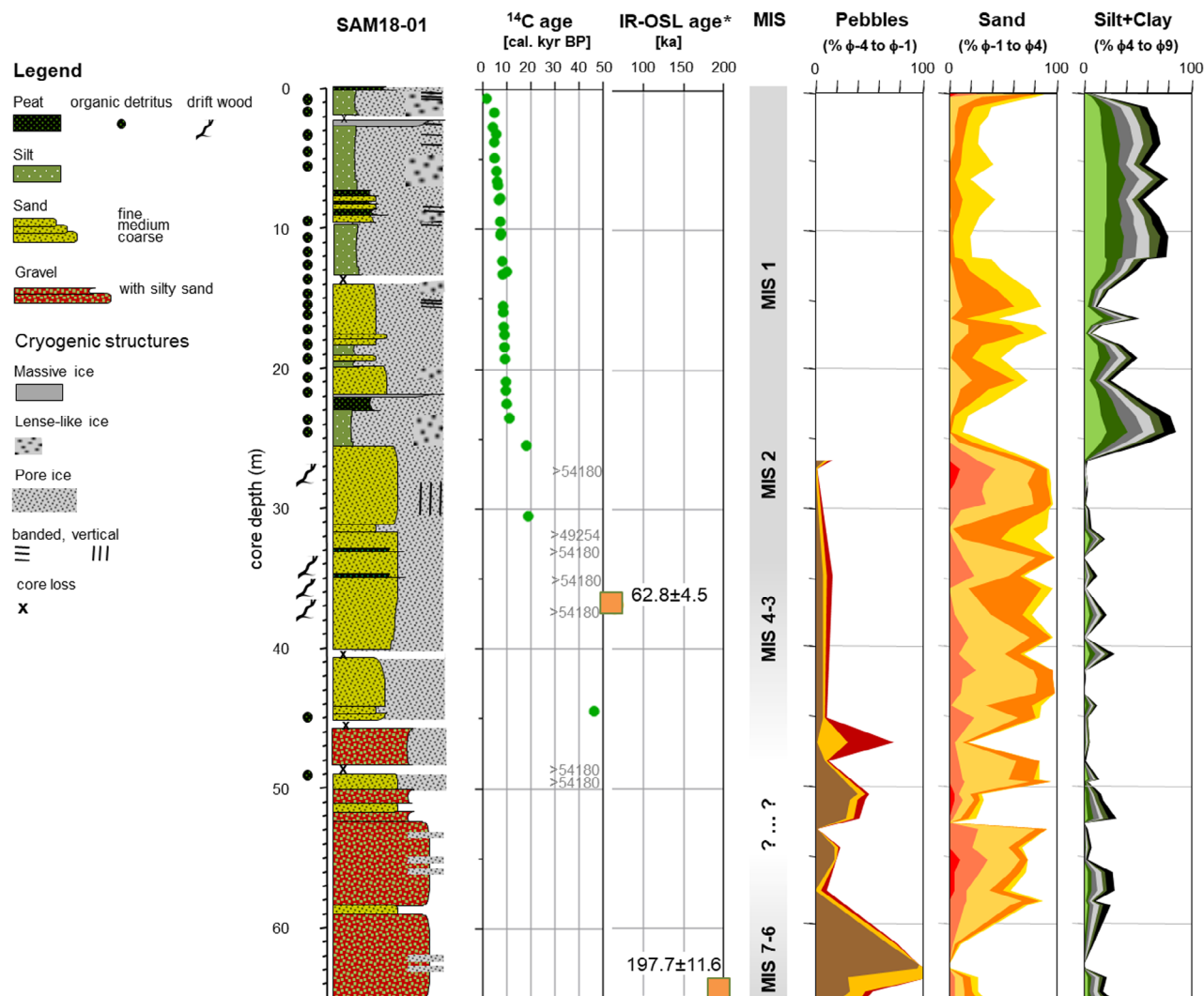


Fig. 2. Cryolithological log of core SAM18-01. The bottom core part at >50 m depth has been retrieved largely unfrozen due to the drilling heat that evolved when entering the pebbly sediments. The age-depth distribution includes two IR-OSL (infrared–optically stimulated luminescence) ages taken from Bolshiyarov *et al.* (2020)*. See text for more discussion. MIS in the lower core part are approximated. Grain-size data with pebble, sand, silt and clay are sorted in phi-steps (medium pebbles = phi-4 to clay = phi 9) and plotted with percentages of each fraction. All fractions build a closed sum of 100%. MIS, marine isotope stage.

50 m depth has been retrieved largely unfrozen, presumably due to the excessive drilling heat that developed when entering the pebbly layers. Above the middle core part, the ice content visibly increases. Between 30.2 m and 28.2 m core depth, centimetre-thick layered vertical bands of ground ice mixed with sand are extraordinary (see core images in Schwamborn *et al.*, 2022). Partly, those vertical bands of ground ice are banded and they also include drift wood fragments (at 28.4 m depth). Above 25 m depth the pore ice frequently turns into a parallel to non-parallel lenticular structure. Between 24.5 m and 21.4 m depth horizontal centimetre-thick bands of ice are developed likely linked with ice segregation (especially between 23.8 m and 23.5 m). In the upper core part at 14.5 m, at 11.9 m, at 10.3 m and 9.7 m the lenticular cryostructure repeatedly shows a distinct horizontal layering. This is also true for core segments between 3.7 m and 3.0 m core depth.

Chronostratigraphy

Two IR-OSL (infrared–optically stimulated luminescence) ages are available from the lower core half (Bolshiyarov *et al.*, 2020). They indicate that the bottom core part reaches back to 197.7 ± 11.6 ka (64.55 m core depth, Fig. 2) and at mid-core the IR-OSL age is at 62.8 ± 4.5 ka (36.53 m core depth).

Radiocarbon dating results (AWI = AMS, KÖPPEN = conventional) with sample information and distribution are shown in Table 1 and Fig. 2. The depth to age distribution illustrates that the finite ages range from bottom to top from 46 520 cal. yr BP (44.25 m core depth) to modern (0.4 m core depth). The ^{14}C age variations are mostly in stratigraphic order and age reversals occur only occasionally; between 50.1 m and 32.25 m core depth out of six samples only one date remains, which points to an early Marine Isotope Stage (MIS) 3 age at the limit of the ^{14}C age scale, whereas the other five samples have too little ^{14}C left for proper age determination. Remarkably, all of those samples with out-of-range ages derive from drift wood fragments. The date 46 520 cal. yr BP (44.25 m core depth) is in conflict with the IR-OSL at 62.8 ± 4.5 ka (36.53 m depth) from overlying sediments. The period between 45 ka BP and 20 ka BP is completely missing from the dating sequence. Between 30.5 m and 25.27 m depth two radiocarbon ages fall into MIS 2, whereas one age

is beyond the ^{14}C age limit. Out of 28 samples with ages belonging to MIS 1, three age reversals can be noticed (Table 1).

Bulk sediment properties

Pebbly sediments of the bottom layers and sandy sediments of the mid-core part show comparably high variation of the elemental behaviour, whereas in the silty layers of the upper core part (<25 to 0 m core depth) the elemental variation is low (Fig. 3). Changing clusters resulting from k-means calculation reflect the fining-up trend of the sediment record: Ca is more enriched in the coarse-grained (pebbly) lower core part, whereas K is relatively enriched in the sandy middle part. Zr is relatively enriched in the fine-grained (silty) upper core part, although less distinctively.

A similar pattern is found with the quartz to feldspar distribution; pebbly and sandy layers in the bottom and middle core part have a higher variation of the quartz abundance, whereas the upper core part shows a fairly stationary load of quartz and feldspar (Fig. 3). Orthoclase to plagioclase varies fairly little in the record. Only in one mid-core sandy layer a pronounced orthoclase maximum is distinct (at 35 m core depth). As with the elemental records the heavy mineral load (amphiboles and pyroxenes) mostly fluctuates parallel to the coarse sand fraction (ϕ_0) (compare with Fig. 2); this is most obvious with peaks in the bottom and mid-core parts. In the upper sediments (above <25 m core depth) the heavy mineral load mirrors the middle sand fraction (ϕ_1). Remarkably, smectite appears in the core only above 25 m core depth, which marks the transition to the upper core silty unit. This is supported by the ratio of clay minerals versus quartz and feldspar, which functions as a grain-size indicator and reflects the combined silt and clay distribution along the core (compare with Fig. 2). Magnetic susceptibility has high values when either fine sand or very fine sand peaks along the record. It is thus an indicator of ϕ_3 and ϕ_2 fraction abundance.

The selection of elements from the XRF data is based on PCA results as shown in Fig. 4. PCA demonstrates that the explained variance for PC1 is fairly low (28.8%), for PC2 it is moderately low (20.2%). The biplot (PC1–PC2) shows positive PC1 loadings of the elements Sr, K and Rb, and negative loadings for the elements Fe, Ti and Zr.

Table 1. Depth, origin, conventional and calibrated ^{14}C ages of SAM18-01 samples.

Lab. no.	Depth (m)	Material	Conv. age (^{14}C yr BP)	\pm (year)	Calibrated age (cal. yr BP)	$2\sigma^+$	$2\sigma^-$
AWI6282.1.1	0.40 to 0.42	Moss fragments	-107	15	Modern		
KÖPPEN1	0.50 to 0.60	Moss fragments	1480	70	1370	1289	1520
KÖPPEN2	1.50 to 1.62	Moss fragments	4080	80	4600	4415	4828
AWI6283.1.1	2.45 to 2.65	Moss fragments	3653	21	3970	3896	4082
KÖPPEN3	2.77 to 3.15	Moss fragments	4680	100	5410	5069	5590
KÖPPEN4	3.55 to 3.73	Moss fragments	4060	80	4570	4303	4830
KÖPPEN5	4.67 to 4.87	Moss fragments	4190	70	4710	4526	4859
KÖPPEN6	5.60 to 5.80	Moss fragments	4770	80	5500	5317	5649
AWI6284.1.1	6.35 to 6.52	Moss fragments	5076	18	5810	5748	5903
KÖPPEN7	6.59 to 6.81	Moss fragments	5340	60	6120	5949	6279
KÖPPEN8	7.74 to 8.00	Moss fragments	6220	100	7110	6805	7413
AWI6285.1.1	7.85 to 8.00	Moss fragments	5730	18	6520	6447	6622
KÖPPEN9	9.20 to 9.41	Moss fragments	6210	70	7100	6907	7269
KÖPPEN10	10.24 to 10.53	Moss fragments	6450	100	7360	7261	7564
AWI6286.1.1	10.38 to 10.55	Moss fragments	6276	21	7220	7163	7255
AWI6287.1.1	12.12 to 12.25	Moss fragments	7139	21	7960	7879	8013
KÖPPEN11	12.69 to 12.99	Moss fragments	8770	130	9830	9542	10 172
AWI6288.1.1	13.00 to 13.18	Moss fragments	7279	19	8110	8022	8170
AWI6289.1.1	15.47 to 15.57	Moss fragments	7429	20	8270	8186	8326
KÖPPEN12	15.47 to 15.91	Moss fragments	7560	100	8360	8174	8587
AWI6290.1.1	16.83 to 16.95	Moss fragments	7775	20	8560	8460	8597
AWI6291.1.1	17.42 to 17.51	Moss fragments	7986	20	8880	8724	8994
AWI6292.1.1	18.30 to 18.40	Moss fragments	8001	20	8880	8772	8998
AWI6293.1.1	19.13 to 19.26	Moss fragments	8155	20	9080	9011	9259
AWI6294.1.1	20.75 to 20.87	Moss fragments	8424	21	9460	9334	9526
AWI6295.1.1	21.40 to 21.50	Wood fragment	8386	20	9430	9312	9480
AWI6296.1.1	22.30 to 22.47	Moss fragments	8757	21	9740	9564	9893
AWI6297.1.1	23.34 to 23.48	Wood fragment	9575	22	10 930	10 756	11 098
AWI6298.1.1	25.27 to 25.44	Wood fragment	14 711	29	18 060	17 892	18 191
AWI6299.1.1	28.20 to 28.50	Wood fragment	>54 180		>54 180		
AWI6850.1.1	30.21 to 30.50	Moss fragment	15 523	139	18 818	18 330	19 110
AWI6301.1.1	32.25 to 32.50	Moss fragments	>49 254				
AWI6302.1.1	35.75 to 35.92	Wood fragment	>54 180		>54 180		
AWI6303.1.1	37.77 to 38.00	Wood fragment	>54 180		>54 180		
AWI6304.1.1	44.25 to 44.48	Moss fragments	44 255	287	46 520	45 883	47 480
AWI6305.1.1	49.60 to 49.75	Wood fragment	>54 180		>54 180		
AWI6306.1.1	49.75 to 50.10	Wood fragment	>54 180		>54 180		

Heavy mineral composition

The very fine sand (fraction 63 to 125 μm , phi 3) has a wide and persistent range of heavy minerals over the record. Greatest heavy mineral loads can be found in the sandy middle unit (maximum of 14%), heavy mineral loads are low in the bottom pebbly part (minimum of 2.2%), and in the upper silt-dominated part (minimum of 0.4%) (Fig. 5). The first group contains amphibole and pyroxene as meta-stable heavy minerals and covers over 50% of all counted non-opaque heavy minerals (Fig. 5). A second group describes a set of meta-stable minerals including epidote, garnet, disthene-kyanite, sillimanite, staurolite, andalusite, chloritoid, muscovite and

biotite. This group makes up to 33% of all counted non-opaque heavy minerals. A third group includes ultra-stable heavy minerals such as zircon, tourmaline and rutile (ZTR), sphene, monazite, and less stable apatite. This group contains up to 15% of the total counted non-opaque heavy minerals. In addition, a minor fraction (<2%) of opaque heavy minerals is available in all samples. Generally, the heavy mineral distribution over the record appears stationary; apart from some accessory minerals (i.e. sillimanite and monazite) much of the spectrum can be encountered at any depth in the record. When entering the upper core unit with silt-dominated sediments there is a slight increase

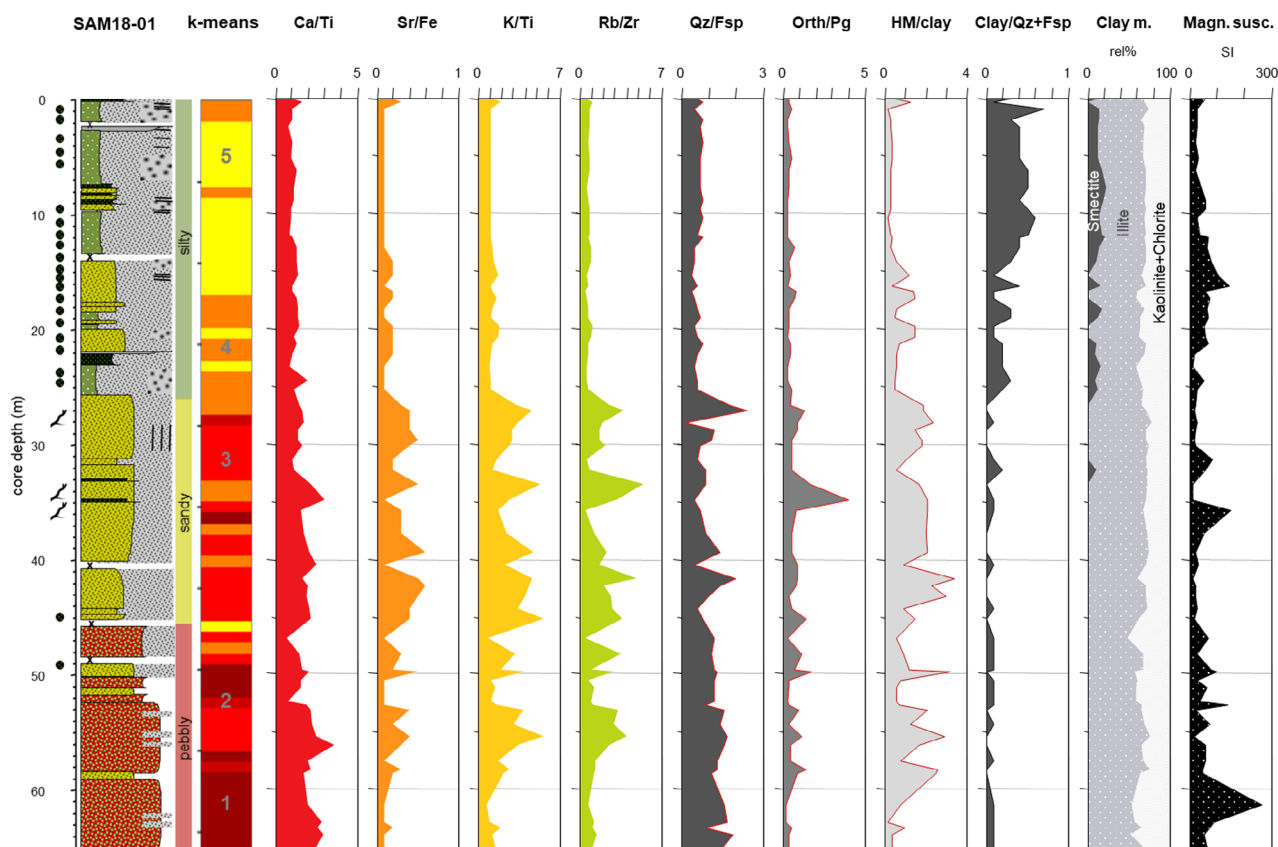


Fig. 3. SAM18-01 core with selected ratios of X-ray fluorescence (XRF) elemental distribution, X-ray diffraction (XRD) mineral distribution, and magnetic susceptibility. K-means cluster (from XRF) are given, in addition: 1 = Fe–Sr–Rb–Zr–Ca; 2 = Fe–Sr–Rb; 3 = Fe–Sr–Rb–K; 4 = Fe–Sr–Rb–Zr; 5 = Fe–Sr–Rb–Zr–K. Abbreviations for minerals: Clay, smectite + illite + kaolinite + chlorite; Fsp, Feldspar; HM, heavy minerals (i.e. Pyroxenes + Amphiboles); Orth, Orthoclase; Pg, Plagioclase; Qz, Quartz.

of pyroxenes at the expense of epidote and apatite.

Complementary first order assessments of rock fragment composition (fraction 2.0 to 3.15 mm) show that the grains originate from various metamorphic, plutonic, volcanic and sedimentary formations (Fig. S1). Monomineralic grains are not observed in this fraction except for some large polycrystalline quartz grains. The grains are mostly subrounded and partly subangular in shape. Sedimentary lithics are mostly rounded to sub-rounded while the volcanic grains can be angular. Metamorphic rock fragments contain lithics from medium to high-grade metamorphic rocks. Polycrystalline quartz grains are associated with metamorphic rock. Plutonic rock fragments dominantly come as granitic lithics. Orbicular granite lithics are observed in some samples. Sedimentary lithics are composed of micro-conglomerate, sandstone, siltstone and

limestone fragments. Volcanic grains are observed with both granular and porphyritic textures (Fig. S1).

Total organic carbon, dissolved organic carbon and hydrochemical properties

TOC, DOC and hydrochemical properties from ground ice are shown in Fig. 6. The ground ice content increases from below 10 wt% in the pebbly core part (note that this part has been extracted largely unfrozen as described above) up to 50 wt% in the sandy mid-core part and has maximum values of over 80 wt% in the silty upper core part. Overall this distribution reflects the fining-upward trend with increasing ice-filled pore space in the sand and silty layers.

TOC distribution remains low in the pebbly core part and varies around a mean of 0.4 wt% (minimum 0.14 wt%, maximum 0.88 wt%),

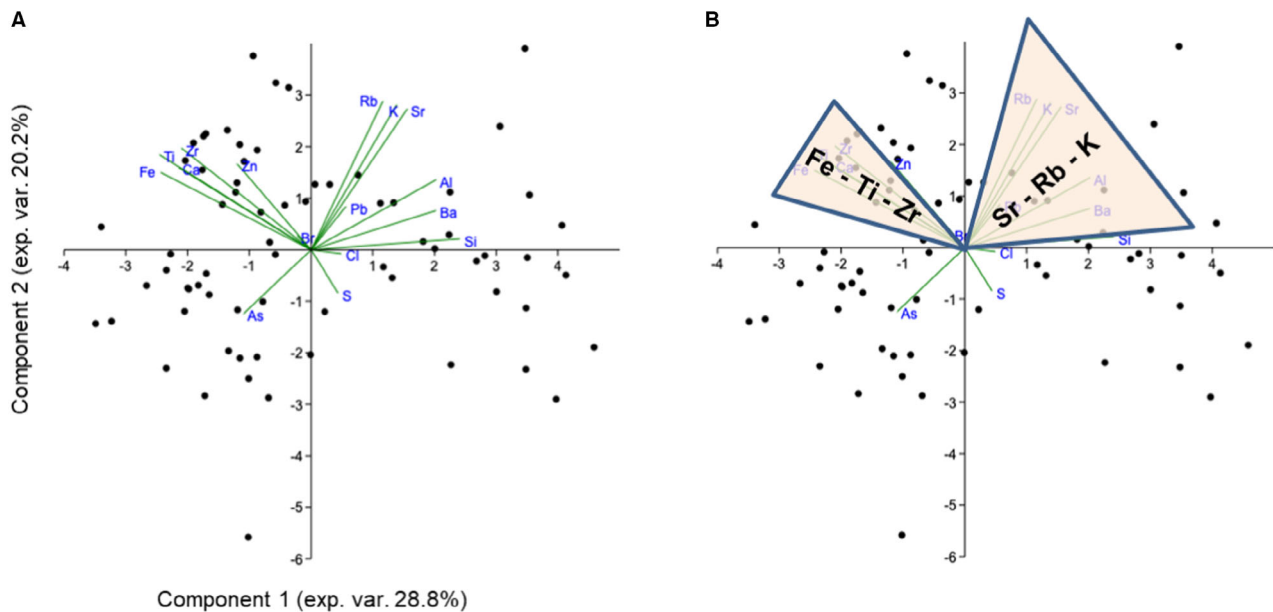


Fig. 4. (A) Biplot (PC1–PC2) showing element correlations and data point distributions of log-ratio transformed X-ray fluorescence (XRF) element intensity records. (B) Dominating elements of PC1 and PC2 are highlighted; the core elemental distribution shows positive PC1 loadings for the elements Sr, K and Rb and negative loadings for the elements Fe, Ti and Zr.

Fig. 6). Bottom-up an initial peak occurs at 49.6 m (2.5 wt%) when first organic detritus macroscopically is observed (see Fig. 2). A **second** (8.5 wt%) and a third (2.7 wt%) pronounced TOC peak appear in the sandy mid-core part at 34.9 m and 32.25 m depth, respectively. In the silty upper core part, the TOC content increases up to a maximum value of 11.9 wt% (at 6.35 m depth), with a mean at 3.9 wt% and a minimum at 1 wt%. Generally, the siltier layers have higher TOC contents, whereas sandy layers tend to have lower than mean values.

The DOC behaviour is trending in a similar way to the TOC distribution even though the two properties differ in physical units; the lower core half is low in DOC (mean 16.1 mg l^{-1}) and the first pronounced peak occurs in the sandy mid-core part at 32.25 m depth (309 mg l^{-1}). At 25.27 m core depth with the onset of the first silty layer the DOC is at maximum (870 mg l^{-1}). In the overlying silty strata, which are richer in detrital organics, DOC remains at higher values and averages at 235 mg l^{-1} . Relative peak positions of DOC and TOC are frequently the same, although the absolute peak behaviour differs from one another (Fig. 6). Interestingly, DOC in the pebble and sand portions is nearly identical

with the average value of the modern-day open water season (18 mg l^{-1} of DOC, Juhls *et al.*, 2020).

In terms of TOC/TN ratios the majority of the organic matter ranges between 10 to 25, outliers have values as high as 29.5 and 47.2 (Fig. 7). In the lower core half, TN values are below the detection limit $>0.1\%$, thus preventing TOC/TN calculations. The organic matter $\delta^{13}\text{C}$ ranges between -23.5% and -29.5% with the majority clustering between -26.0% and -28.0% (Fig. 7).

The ground ice pH is alkaline for much of the record with values up to 8.6 (Fig. 6). A prominent exception is observed between 6.85 m and 3.83 m core depth, where the organic-rich silty layers have acidic pH with values between 5.5 and 6.0. The EC overall shows a decreasing trend from bottom to top core; within the pebbly layers the EC has an average value of $1030 \mu\text{S cm}^{-1}$, in the sandy mid core unit it averages at $740 \mu\text{S cm}^{-1}$, in the upper silt unit it averages at $430 \mu\text{S cm}^{-1}$. An exceptional high peak of $3180 \mu\text{S cm}^{-1}$ occurs at 25.27 m core depth at the transition from the sandy to the overlying silty unit. EC values from the top core silty unit overlaps fairly well with the range of the annual cycle as recently measured (Fig. 6, Juhls *et al.*, 2020). Similar to EC, the measured

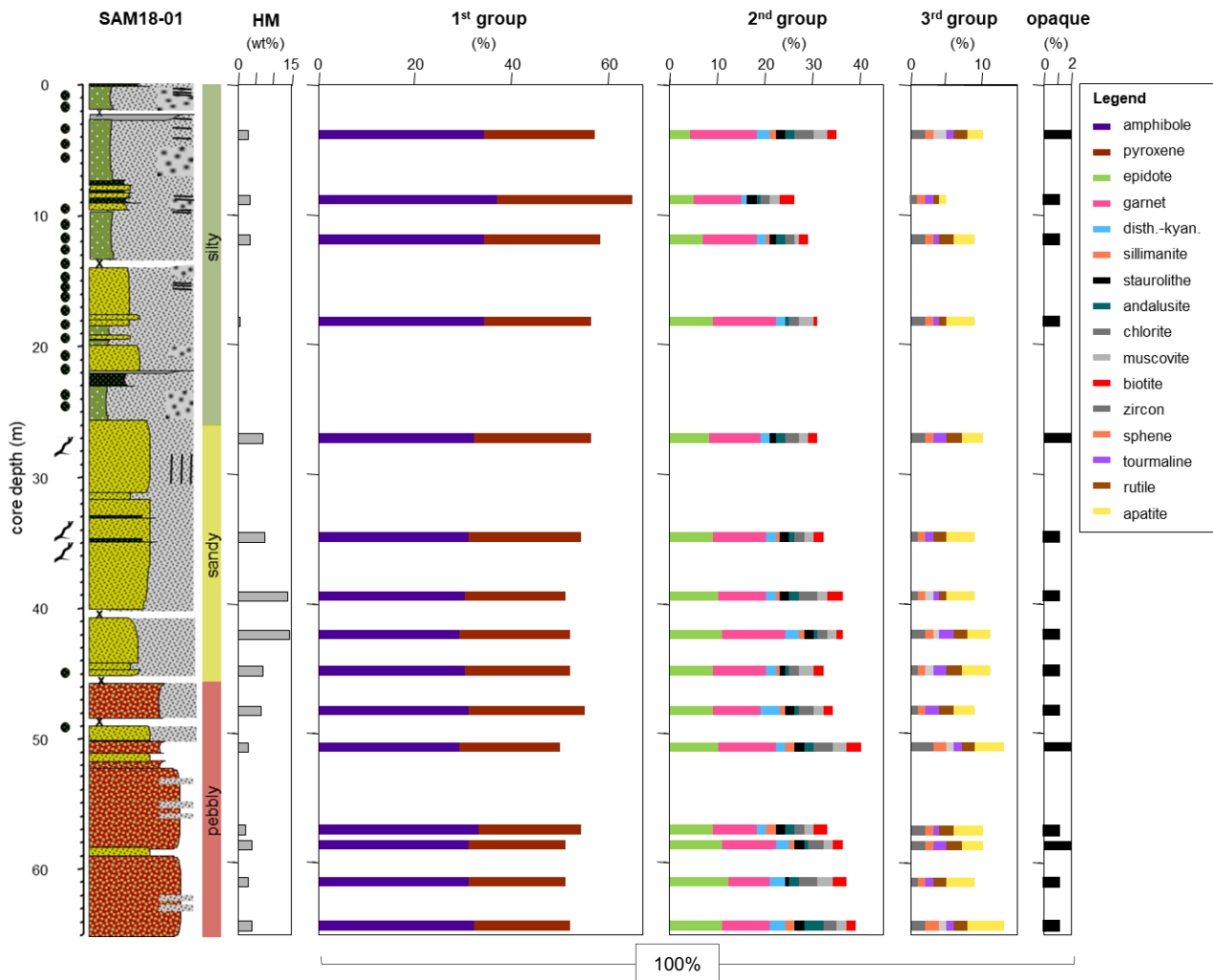


Fig. 5. Heavy mineral compositions of core SAM18-01 showing the relative abundance changes. HM = heavy mineral load from fraction 63 to 125 μm expressed in weight-percent (wt%). Minerals of first group + second group + third group + opaque build a closed sum of 100%.

anions (i.e. chlorine and sulphate) decrease from bottom to top; in the lower core half values range between 100 mg l^{-1} and 10 mg l^{-1} , in the upper core half values are $<10 \text{ mg l}^{-1}$.

The covariate stable oxygen and hydrogen isotopes ($\delta^{18}\text{O}$, δD) have little variation between 65 m and 35 m core depth (mean $\delta^{18}\text{O} = -20.7\text{‰}$, mean $\delta\text{D} = -160.2\text{‰}$), they expose a marked minimum peak at 27 m core depth ($\delta^{18}\text{O} = -30.1\text{‰}$, $\delta\text{D} = -237.7\text{‰}$) before averaging at more heavy values between 22 m and 0 m core depth (mean $\delta^{18}\text{O} = -17.8\text{‰}$, mean $\delta\text{D} = -136.8\text{‰}$). Similarly, the *d-excess* range is narrow between 65 m and 32 m core depth (mean *d-excess* = 5.8‰), the lowest *d-excess* values occur at 29.7 m depth (-11.9‰). High *d-excess* values are observed in a

peaty layer at 22.3 m (+13.1‰) and in the upper 1 m of core (+10.6‰ and +14.6‰). Other values in the upper silty unit range around 5.3‰. At 6.35 m core depth, where the pH is low, an exceptional relative *d-excess* minimum of -0.7‰ is observed.

In a co-isotope presentation the stable water isotope composition illustrates that much of the ground ice falls below the GMWL (global meteoric water line; Craig, 1961). The minimum values from between 32 m and 24 m core depth have a distinct offset from all other values. Where *d-excess* is highest; i.e. between 23 m and 22 m core depth and from the active layer (Fig. 6), values are located above the GMWL (Fig. 8).

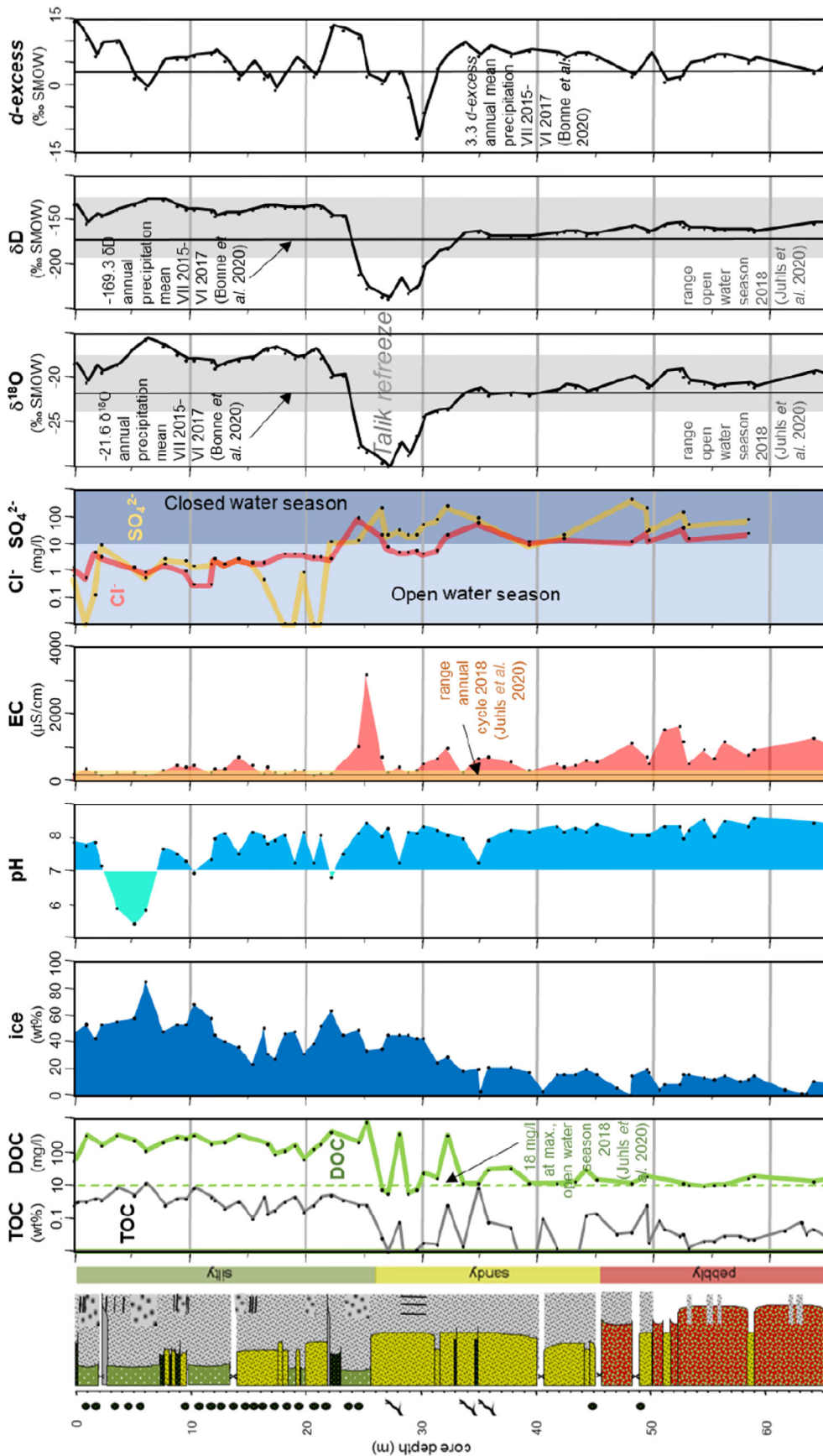


Fig. 6. SAM18-01 core with total organic carbon (TOC) and hydrochemical properties. Values of modern-day Lena River dissolved organic carbon (DOC) and electrical conductivity (EC) are given based on Juhls et al. (2020), modern-day Lena Delta $\delta^{18}\text{O}$ and δD from precipitation is based on Bonne et al. (2020), Lena Delta $\delta^{18}\text{O}$ and δD from river water of the open water season is based on Juhls et al. (2020). Coloured background in Cl^- and SO_4^{2-} column is defined using data from Juhls et al. (2020).

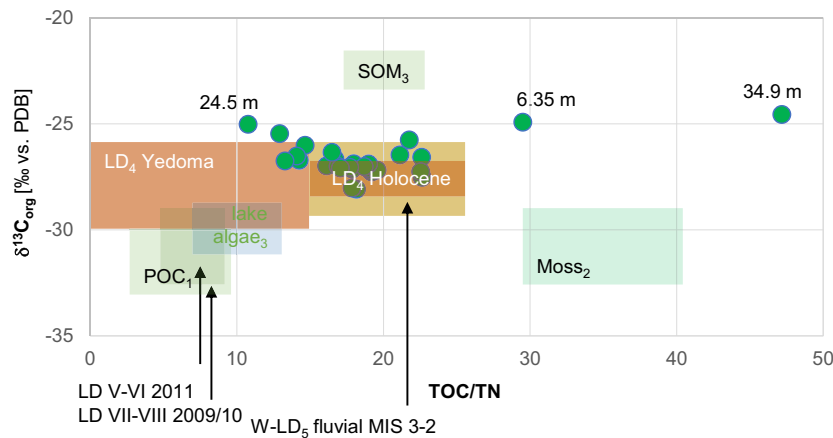


Fig. 7. Biplot of $\delta^{13}\text{C}$ and TOC/TN (total organic carbon/total nitrogen) from SAM18-01 bulk organic matter (green dots). Colourized rectangles for comparison; POC_1 = particulate organic carbon measured from fluvial samples of the Lena Delta (Winterfeld *et al.*, 2015), Moss_2 from the central Lena Delta (Zibulski *et al.*, 2017), lake algae₃ and SOM_3 = soil organic matter from Transbaikalia (Prokopenko *et al.*, 1993), LD_4 = Lena Delta Yedoma (MIS 3–2) and Holocene cliff exposure (Wetterich *et al.*, 2008, 2020), W- LD_5 = western Lena Delta fluvial deposits (MIS 3–2) from cliff exposure (Schirrneister *et al.*, 2011).

DISCUSSION

Sediment history

Palaeogeographical understanding of the study area has developed over many years and palaeoclimate and palaeoenvironment reconstructions are available from various sites along the Laptev Sea southern margin. In an exemplary way Schirrneister *et al.* (2002) summarize multiproxy data to interpret palaeoclimate and sedimentation history back to MIS 4. Those authors use exposure samples of unconsolidated ice-rich permafrost from the Bykovsky Peninsula, which is located 120 km south-east from the Lena River delta apex. Wetterich *et al.* (2008) back to *ca* 100 ka and Wetterich *et al.* (2020) back to 52 cal. kyr BP use a similar approach to study neighbouring islands in the Lena Delta (Kurungnakh Island; 10 km south-west from the coring site, Sobo Island; 60 km north-east from the coring site). Schirrneister *et al.* (2003, 2011) studied several islands in the western Lena Delta (Turakh, Ebe Sise, Khardang, Djangilakh and Kurungnakh) with maximum ^{14}C ages of *ca* 53 kyr BP and U/Th ages of *ca* 100 kyr. A reconstruction of palaeoclimate and palaeoenvironment back to MIS 7 (221 ± 27 ka) is presented in Wetterich *et al.* (2019) where ice-rich permafrost from Bol'shoy Lyakhovsky (New Siberian Islands) has been studied, this site is located 500 km north-east of the core location. In the

western Laptev Sea, at Cape Mamontov Klyk (330 km north-west of the study site) ^{14}C ages at coast exposures go back to *ca* 44 kyr BP at 10 m above sea level and OSL ages go back to *ca* 57 kyr at 1.3 m above sea level and in a core *ca* 96 kyr at 34 m below sea level. A core drilled 12 km off the coast was ^{14}C -dated back to *ca* 44 kyr BP in 44.7 m depth below sea level and *ca* 148 kyr (59.3 m depth below sea level) by quartz OSL and *ca* 111 kyr (77 m depth below sea level) by IR-OSL on feldspars (Schirrneister *et al.*, 2008; Winterfeld *et al.*, 2011). All of these studies include multiproxy data from various sediment and ground ice analyses, various dating techniques, and palaeoecological analyses.

The bottom part of SAM18-01 with pebbly sand over a core length of 20 m is interpreted to represent fluvial bedload from the period of *ca* MIS 7 to MIS 4 (IR-OSL ages: 197.7 ± 11.6 to 62.8 ± 4.5 kyr, Bolshiyarov *et al.*, 2020). In this unit, times of accumulation and erosion are poorly resolved. For MIS 5e a global sea level higher than modern has been reconstructed (Spratt & Lisiecki, 2016). This means that any deposits at the coring site likely have been part of a shallow Laptev Sea margin of that time. Following glacial regression starting at MIS 4 these sediments likely have been eroded, or reworked, and mixed or replaced by successive Lena bedload. On the other side, it is known from terrestrial Eemian deposits, which have been found on Bol'shoy Lyakhovsky and Oyogoss Yar

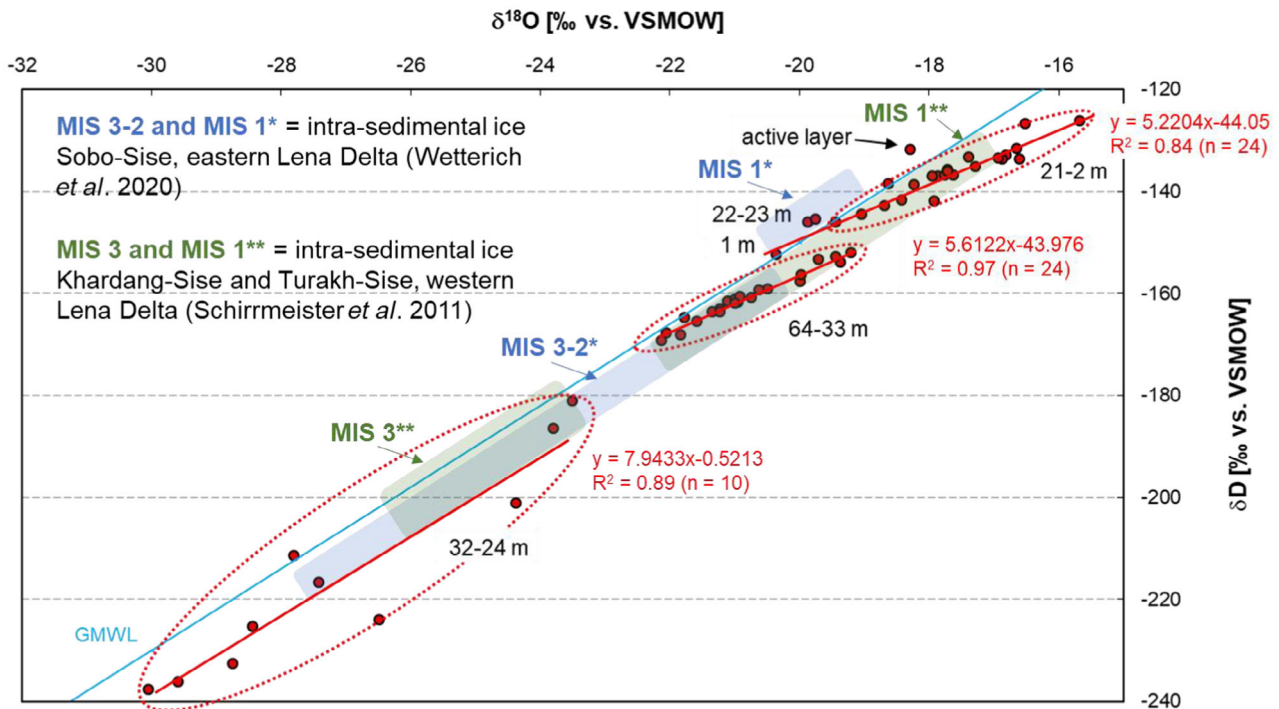


Fig. 8. Biplot of $\delta^{18}\text{O}$ and δD from SAM18-01 ground ice (red dots). Depth information and dashed circles indicate particular core portions. Red lines mark freezing slopes (with values) for corresponding core parts. Shaded areas in blue and green represent ground ice composition of different ages from elsewhere in the Lena Delta (Wetterich *et al.*, 2008, 2020; Schirrmeister *et al.*, 2011). GMWL, global meteoric water line according to Craig (1961).

(500 km to the north-east from the core location), that the Laptev Sea at that time was located further north. Likely this apparent contradiction might have a neotectonic reasoning (Kienast *et al.*, 2008; Wetterich *et al.*, 2009; Kienast *et al.*, 2011). In addition, changes of sea level, air temperature, radiation and precipitation patterns, hydrology, and vegetation need to be considered for a long period such as between MIS 7 and MIS 4 (Mock *et al.*, 1998) and which might have their impact on the Lena discharge regime.

The inversion of the ^{14}C age 46 520 cal. yr BP (44.25 m core depth) with regard to the IR-OSL age at 62.8 ± 4.5 ka (36.53 m core depth) from overlying sediments might be explained by sample contamination; it cannot be fully ruled out that in the course of the drilling progress the dated sediment has been imported from upside to down during the technical progress. Moreover, problematic discrepancies between radiocarbon and luminescence ages from permafrost are also known from elsewhere; as discussed in Schirrmeister *et al.* (2011) potential reasons concern different physical effects for dating with

correspondingly different uncertainties and permafrost-specific cryogenic processes. They perhaps mobilize and relocate sediment or affected mineral crystal parameters because ice grows within pore spaces. A final judgement about this particular age inversion must remain open for now.

Interestingly, in an early work from Puminov (1960) it has been interpreted that during the last interglacial (MIS 5, Kazantsevo = Eemian and Early Weichselian) the lower Lena has used parts of the Olenek River valley further west before entering the Laptev Sea lowland. This study is based on relative dating of Olenek River terrace morphology and the associated mineral compositional change. Accepting the views of Puminov (1960) about the deposits' age and their genesis and applied to the SAM18-01 record, this argues for a hiatus for that period, since the Lena mouth and the Olenek mouth areas are located 200 km apart. Dating and mineral change of the lower core part do not resolve any environmental change, which might be associated with this; for example, alien mineral loads from more local sources at that

time. In addition, an inferred hiatus (according to Puminov, 1960) or a possible mineral change and associated changes to rates of erosion brought on by climatic variations are buffered during transport in large rivers and may not be recognizable in the sedimentary record; large-scale fluvial systems lead to prolonged residence times, which can exceed even glacial–interglacial cycles (Ben-Israel *et al.*, 2022).

The sandy middle core part represents the fluvial saltation load from the period MIS 3 to MIS 2. In this unit and valid again for 20 m of core, times of accumulation and erosion are poorly resolved. The river history of that period is understood to include times of fluvial channel migration and changes in local discharge dynamics. In contrast, the top core silty part, which is mixed with organic detritus, accumulated fairly continuously over 25 m of the core as suspension load during MIS 1. The accumulation of the suspension load is associated with the base level adjustment in the course of post-glacial global sea-level rise, thereby controlling the Lena River deltaic position in the Laptev Sea lowland. According to the transition from sandy to silty sediments the silty floodplain environment started to establish around the onset of the Holocene. As known from marine sediment records from the Laptev Sea and modelling efforts using glacial isostatic adjustment, the modern-day sea level established at 6 to 5 kyr BP (Bauch *et al.*, 2001; Klemann *et al.*, 2015). The early establishment of floodplain conditions at the core site pre-dating the advent of the sea level might be due to shallow bathymetry in the river branch, decreasing stream power or local discharge rerouting. River-ice jamming during the spring river break-up is known to initiate restructuring of the hydrographic network (Fedorova *et al.*, 2015). Other palaeovalleys, presumably associated with the Last Glacial Maximum (LGM), extend up to 200 to 300 km north of the modern Arctic shoreline (Holmes & Creager, 1974) and have been verified using seismic profiling (Kleiber & Niessen, 1999; Rekant *et al.*, 2015).

Although the global scale ice melting markedly decreased after mid-Holocene time, modelling suggests another *ca* 6 m of sea-level rise at the mouth of the Lena River until 3 ka (Whitehouse *et al.*, 2007). This matches findings that the last 3000 years witnessed formation of the major portion of the above-water territory corresponding to the north-eastern sectors of the Lena River delta (Korotaev, 2011).

In Holocene time, the vast delta plain formed in various depositional lobes based on radiocarbon age distribution in floodplain levels across the modern-day delta (Pavlova & Dorozhkina, 2000; Bolshiyarov *et al.*, 2015; Fig. 1D). The deltaic accumulation frames and partly erodes remnants of late Pleistocene origin (MIS 4–3 ‘Yedoma’ deposits in the south and the north-east, MIS 3–1 fluvial deposits on Arga Island in the north-west) at the Laptev Sea southern lowland (Schwamborn *et al.*, 2002; Schirrmeister *et al.*, 2011; Fig. 1D). Yedoma deposits are syngenetically frozen, ice-rich and silt-dominated permafrost, which is widely found in northern Siberia, Alaska and north-west Canada (Schirrmeister *et al.*, 2013; Murton *et al.*, 2015; Strauss *et al.*, 2021b).

The wide mineral spectrum remains stationary over the record and reflects well the three major geological physiographic provinces that underlie the catchment; the Siberian Palaeozoic sedimentary basin, the Precambrian Aldan shield, and the collisional suture of the Verkhoyansk Mountain belt with Mesozoic tuff and detrital deposits (Kleiber & Niessen, 2000; Potter *et al.*, 2001; Prokopiev *et al.*, 2009). Correspondingly, the inspected rock fragments document an origin from a variety of metamorphic, plutonic, sedimentary and volcanic formations (Fig. S1) underlying the catchment. Remarkably, the Lena River heavy mineral spectrum is also found in a MIS 3–1 formation, which builds a prominent elevated island (Arga Island) to the north-west of the modern-day delta and accordingly this island is interpreted to represent a palaeo-fluvial stage of the Lena at that time (Schwamborn *et al.*, 2000, 2002; Schirrmeister *et al.*, 2011, 2022). However, the Lena heavy mineral composition does not match with MIS 4–3 Yedoma, which is cropping out at the southern edge of the delta; for example, closest to our drilling location are Kurugnakh Island (Wetterich *et al.*, 2008) and Sobo Island (Fuchs *et al.*, 2020; Wetterich *et al.*, 2021). Apparently, Yedoma formations in north Siberia have received their sandy fractions from bordering uplands instead (Schwamborn *et al.*, 2002; Siegert *et al.*, 2002; Schirrmeister *et al.*, 2003; Schirrmeister *et al.*, 2020). The Verkhoyansk Mountain belt is known to have glacial advances at MIS 5d, MIS 5b, MIS 4 and MIS 3 crossing the Lena River middle reaches (e.g. Stauch & Lehmkuhl, 2010). Also from Laptev Sea sediments it is known that at least at 13 kyr cal. BP a freshwater pulse from the Lena River entered the shelf waters and clearly altered the offshore

hydrochemical composition (Spielhagen *et al.*, 2005). However, the SAM18-01 record from the lower reaches does not resolve any of these events in terms of mineral change. Exceptionally, the number of pyroxenes slightly increases in the upper core part, whereas the amount of epidote and apatite minerals slightly decreases at the same time; but this might be explained with a process change rather than a source change. The sedimentary environment decreases in average grain size and turns from a fluvial channel with a sandy load to an alluvial floodplain with a suspension load. More epidote and apatite particles still may be present in the sediment, but might be found in the silty fraction, which is not studied here.

Expressed in TOC/TN and $\delta^{13}\text{C}$ values, most of the organic matter above 25 m core depth resembles properties of palaeo Lena River deposits (MIS 3–2) known from a western delta site (Schirrneister *et al.*, 2011) and late Pleistocene Yedomia (MIS 3–2) deposits and Holocene deposits known from elsewhere in the delta (Fig. 7, Wetterich *et al.*, 2008, Wetterich *et al.*, 2020). Individual samples with high TOC/TN are associated with drift wood particles (Meyers & Teranes, 2001). Typical values of moss (Zibulski *et al.*, 2017) as known from the central delta (Samoylov Island) or POC (particulate organic carbon) as known from river water sampling (Winterfeld *et al.*, 2015) are not met with SAM18-01 bulk organic matter. This is also true for Transbaikalian lake algae (Prokopenko *et al.*, 1993), which all have lighter isotope signatures with $\delta^{13}\text{C} < -29\text{‰}$. If initially available at all, biodegradation might soon alter the isotope signature of algae and moss towards more heavy values once microbial decomposition affects the material after deposition at the site (Strauss *et al.*, 2015; Vonk *et al.*, 2016; Natali *et al.*, 2020).

The depositional change from a fluvial environment (pebbly and sandy layers) to a more alluvial environment with suspension load sedimentation is also reflected in the decreasing light soluble load within the silty top. Whereas ionic concentrations $>10 \text{ mg l}^{-1}$ are typical for the closed water season (for example, chlorine and sulphate in Fig. 6), ionic concentrations $<10 \text{ mg l}^{-1}$ are associated with the open water season when much of the snowmelt dilutes the river discharge (Juhls *et al.*, 2020). It is only during the open water season, when suspension load is distributed and deposited in the delta plain or at overbank positions. The change from high to low solute values is also mirrored in the

upcore EC distribution with higher than average values in the pebbly and sandy core parts and low EC values in the silty core part, which are similar to modern-day hydrochemical compositions (Juhls *et al.*, 2020). The exceptional EC maximum at 25 m core depth is discussed further below.

Permafrost formation

In a co-isotope plot, the stable water isotope composition illustrates that much of the SAM18-01 ground ice falls below the GMWL (global meteoric water line, Craig, 1961, Fig. 8). Three clusters are apparent; intermediate $\delta^{18}\text{O}$ and δD (and moderately variable *d-excess*) values prevail in the lower core half (between 64 m and 33 m depth), lowest $\delta^{18}\text{O}$ and δD (and highly variable *d-excess*) values are found at mid-core (between 32 m and 24 m depth), highest $\delta^{18}\text{O}$ and δD (and moderately variable *d-excess*) values are detected in the upper core part (between 21 m and the active layer, see Fig. 6). The freezing process is known to cause a deviation from the GMWL along a line with a lower slope (a so-called freezing slope) that can be diagnostic of the conditions prevailing during freezing (Lacelle *et al.*, 2004). During equilibrium freezing, the value of the $\delta^{18}\text{O}$ – δD regression slope differs from that of the GMWL, because of different isotopic fractionation coefficients (for ^{18}O and D) during the water–ice phase transition than is the case for the water–vapour fractionation. This is true for the bottom core part (freezing slope $y = 5.6$) and the upper core part (freezing slope $y = 5.2$) as seen in Fig. 8. It is not true for the mid-core isotope minimum, which has a slope parallel to the GMWL ($y = 7.9$). This argues for an open system freezing process, since Lacelle (2011) concluded that ice produced by freezing of precipitation or meltwater under equilibrium conditions in an open system will tend to have a slope near or >7.3 . In this way there should be a wider lateral connection to neighbouring water reservoirs, when the mid-core isotope minimum was formed. In contrast, slopes around 5 to 6 at the bottom and the top core suggest a non-equilibrium freezing in a closed system, when permafrost formed (Fritz *et al.*, 2011). It is interpreted from this that after a river arm migration talik sediments started to freeze over from two sides; from the exposed top of the section and from below, where at greater depths permafrost was already established. However, in this

context samples from core SAM18-01 do not contain ground ice of the final stages of refreezing, which would be accompanied by very low delta and high *d-excess* values.

Except for the mid-core isotope minimum, much of the δD values from SAM18-01 ground ice fit into the range that is known from modern-day Lena discharge during the open water season (−190 to −130‰, Juhls *et al.*, 2020, Fig. 6). It is also overlapping with the mean modern-day precipitation values over the delta (Bonne *et al.*, 2020). Yet, in the upper 23 m a distinct offset towards less negative δD values is obvious. In contrast, the $\delta^{18}O$ values fit into the modern-day range only in the lower core half, whereas the upper 25 m of core are enriched in ^{18}O . When comparing SAM18-01 ground ice with other intrasedimental ground ice sampled in the western and eastern Lena Delta (Wetterich *et al.*, 2008, 2020; Schirrmeister *et al.*, 2011) an offset between lighter MIS 3–2 values and more heavy MIS 1 values is confirmed (Fig. 8); especially the upper 23 m of core SAM18-01 overlaps with known MIS 1 values, whereas the lower core half largely overlaps with the MIS 3–2 range (Wetterich *et al.*, 2008, 2020, Schirrmeister *et al.*, 2011). It implies that the freezing history of the site likely took place with a pronounced temporal offset after the fluvial sedimentation. In that sense, specifically the lower core half experienced a distinct post-sedimentary permafrost formation. A more complex history of multiple freezing must be assumed for the upper core part, as indicated by the moderately variable *d-excess*, which is discussed further below.

Related to humidity this also argues: (i) for a connection with higher temperatures in MIS 1 time, which would allow to carry and rain out of isotopically heavier precipitation over the Lena River catchment; or (ii) pronounced evapotranspiration effects, which are presumably negligible in the foremost fluvial environment. Alternatively, elevation can play a role, but likely does not in the extended Lena catchment. Finally, a source area change cannot be ruled out, because of potentially changing atmospheric vectors over the Quaternary. The presently dominant Siberian High can differ in the past, leading to the possibility of numerous different patterns of spatial climatic responses; at various times during the late Quaternary, external climatic controls such as ice sheet size, sea ice extent, land–sea distribution and insolation were dramatically different than today and modifying the atmospheric pattern (Mock *et al.*, 1998). For

example, when regarding Holocene versus MIS 3 winter conditions differences in moisture transport paths have been described by Meyer *et al.* (2002). Permafrost outcropping on nearby Bykovsky Peninsula (120 km south-east from the coring site) has distinctly lower MIS 3 delta values and *d-excess* when compared with Holocene permafrost. Overall, the contrast between cold-climate (glacial time) and rather temperate (interglacial) Lena river discharge is seen as the controlling factor; it causes the isotopic composition to shift to more positive values in the upper core, since temperature is one of the controlling factors of stable water isotope fractionation and can be tracked back in time also in ground ice records (Porter & Opel, 2020).

In addition, the *d-excess* gives evidence on the deviation from the GMWL and helps to elucidate the kinetic (i.e. non-equilibrium) fractionation processes. On a global scale, the *d-excess* is affected by relative humidity during the formation of primary vapour masses and for precipitation averages +10‰ on global average; the *d-excess* is reduced to values near 0‰ and lower by non-equilibrium fractionation during subsequent phase changes, including evaporation or freezing of moisture when ground ice forms (Lacelle *et al.*, 2004). The varying *d-excess* values over the record range between more than 14‰ and less than −11‰ (Fig. 6) and indicate that during the permafrost formation much of the ground ice likely froze and thawed several times. Decreasing *d-excess* may also be related to greater input from rain rather than snow into the ground ice system, because rain may be influenced by secondary evaporation and by the recycling of regional moisture, for example in the tundra (Kurita *et al.*, 2003). Especially at 23 to 22 m core depth secondary fractionation can be detected with δ values above the GMWL (Fig. 8). It is known from an Alaska near-surface ground ice formation, which was fed by palaeoprecipitation (Meyer *et al.*, 2010), that the thermal change across the Younger Dryas–Holocene transition is expressed in an increasing *d-excess* from 5 to 10‰. Low *d-excess* in MIS 3 ground ice and high *d-excess* in MIS 1 winters have been described for permafrost exposed in the south-eastern vicinity of the Lena River delta (Meyer *et al.*, 2000). Similarly, a distinct warming took place, when sediments at 23 to 22 m depth were deposited as they are dated to the onset of the Holocene (Table 1) and that thermal change may have caused a high *d-excess*. Low *d-excess* and low pH between 6.3 m and 3.8 m

depth might be related to snow conditions at that time (Schwamborn *et al.*, 2014) or possibly a higher load of humic acids in the permafrost, but this interpretation is premature. This is true also for the upper one metre of core, which still is undergoing thaw and freeze cycling, making an interpretation of high *d-excess* there inappropriate by now. Juhls *et al.* (2020) measured the modern-day stable water isotope composition of the Lena River; for the open water season the fluvial $\delta^{18}\text{O}$ ranges between -23.7‰ and -17.5‰ and the δD ranges between -180‰ and -130‰ . Remarkably, in this way nearly all values from SAM18-01 ground ice can be reproduced from this range (Fig. 6).

River branch re-routing has been suggested by Are & Reimnitz (2000) to be a typical feature of an Arctic delta setting; apart from internal deltaic dynamics fluvial branches may be redirected, when river ice jamming builds up obstacles during times of spring meltwater discharge. This will force the river discharge to divert and to establish a new river channel. With some temporal delay, the underlying river talik will follow to the new

position of the migrated river branch. The prior talik location will freeze over below the abandoned channel. In terms of a successive freezing process ^{18}O will freeze in before ^{16}O and create a distinct ground ice stable isotope minimum following Lacelle *et al.* (2004). The first ice issued from this water has a $\delta^{18}\text{O}$ of -22‰ and, as freezing continues and removes the heavy isotopes from the residual water, each successive freezing fraction produces isotopically lighter ice (Dyke, 2000). This freezing process will take place both from below and above the talik. A scheme of this situation is given in Fig. 9. The $\delta^{18}\text{O}$ - δD minimum at mid-core of SAM18-01 is interpreted to result from a talik refreeze. Freezing from two sides may produce a central layer (like in a sandwich) where light soluble salts are enriched and which is the last layer to freeze over before permafrost formation is completed. Such a peak with high EC ($3180\ \mu\text{S cm}^{-1}$) is found at 25.3 m core depth and it overlaps with the prominent stable isotope minimum found at the same depth. Interestingly, this also coincides with the vertical ice bands in the corresponding

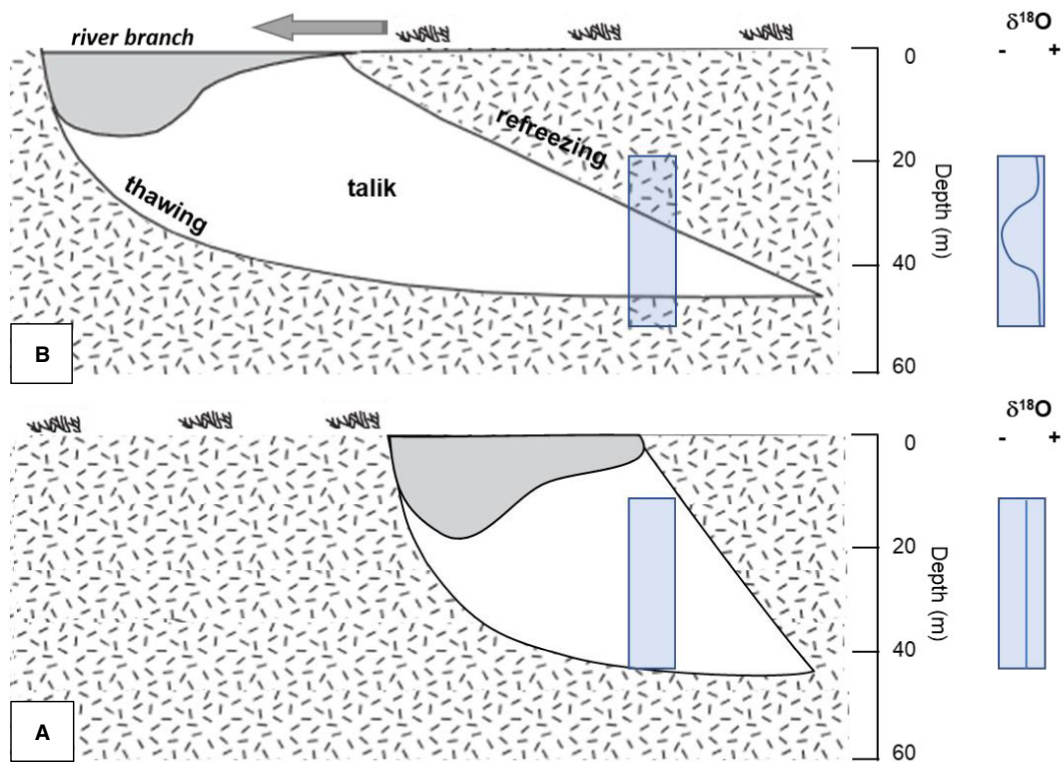


Fig. 9. Predicted talik migration below a migrating river branch and the associated ^{18}O isotope minimum at the refreezing front (modified from Dyke, 2000). (A) Initial situation with talik sediments and levelled ^{18}O isotope distribution below the river bed. (B) Refreezing from top and bottom favours a heavier isotope composition to freeze out first and deplete in ^{18}O in the part that freezes out last.

sediments. Following French & Shur (2010) the freezing of sediment in a lake talik from the side (parasynogenesis) can result in upright cryotextures. From its stratigraphic position at earliest an early Holocene age is assumed for the talik refreeze.

Tectonic setting

Onshore and offshore geological prospecting shows that the middle Pleistocene to Holocene clastic fluvial and deltaic Lena River deposition

is blanketing Proterozoic rock and extensional and normal fault lines are interpreted to intersect the delta (Franke & Hinz, 2009; Harrison *et al.*, 2011; Drachev, 2016; Fig. 10). Both compression and dilatation patterns are reported in the area with earthquake magnitudes between 5 and 6 (Avetisov, 1999; Lukina *et al.*, 2003; Fujita *et al.*, 2009). This implies that late Quaternary block movement at the boundary between the Eurasian and the North American plates cannot be excluded to have had an impact on river routing in the Laptev Sea lowland. The third

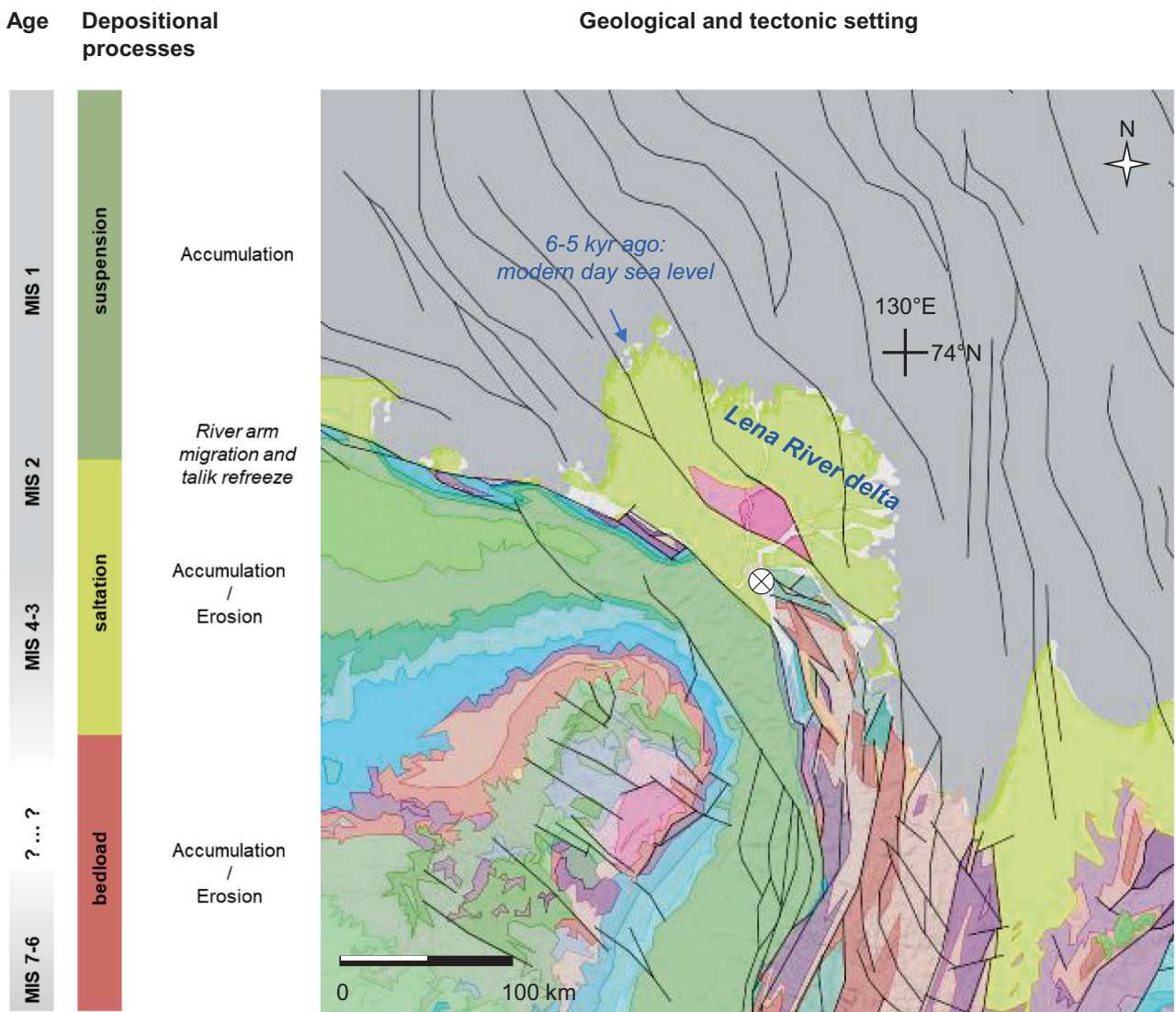


Fig. 10. Main depositional processes in the lower Lena River over late Quaternary time (left part), and tectonic setting (right part); Pleistocene–Holocene clastic fluvial and deltaic deposition (yellow colours) overlies Proterozoic rock (magenta colours) north of the Phanerozoic Siberian mainland (multi-coloured). Note, extensional fault lines intersect the Lena River delta, compressional fault lines dominate the Siberian mainland. The circle marks the core position. Background geological map after Harrison *et al.* (2011).

terrace in the Lena River delta (MIS 4–3) can be subdivided into two areas due to a considerable difference in altitude (more than 20 m) between the western and the eastern sector; this has been linked to syn-depositional or post-depositional vertical tectonic movements (Grigoriev, 1993). In addition, isostatic compensation movements following the retreat of the large ice caps during the Late Glacial may have led to additional amplification of neotectonics processes (Whitehouse *et al.*, 2007).

CONCLUSIONS

A 65 m long sediment core (SAM18-01) from the central Lena River delta has three main units; the bottom part (65 to 45 m) consists of pebbly sand representing the time-discontinuous Lena River bedload of the period between *ca* MIS 7 at maximum to MIS 4. In this unit times of accumulation and erosion are poorly resolved, a hiatus for the last interglacial is likely. The middle part (45 to 25 m) is dominated by sandy layers representing Lena River saltation load from the period MIS 3 to MIS 2. In this unit again, times of accumulation and erosion are poorly resolved. The upper core part (25 to 0 m) is silt-dominated with pronounced occurrence of organic detritus and which accumulated fairly continuously over the Holocene.

Based on a set of sediment and ground ice properties the following conclusions are drawn:

- The fine sand mineral composition remains stationary over the record; it does not resolve hinterland glaciation events, although they are known to take place. Major changes in the drainage path of the Lena River are not detectable.
- A prominent ground ice stable isotope minimum ($\delta^{18}\text{O}$, δD) at mid-core (early MIS 1) highlights a river arm migration that involved the refreezing of the underlying river talik. This is regarded a typical feature within an Arctic river delta plain. Epigenetic freezing took place in the former talik deposits at the coring site.
- After river arm migration a floodplain environment established at the onset of the Holocene. The accumulation of the organic-rich silty to clayey suspension load is likely linked to a fluvial discharge decrease, to the shallowing of the depositional site in the course of a river arm rerouting possibly after river ice jamming, and the base level decrease on the shallow Laptev Sea shelf after the post-glacial sea-level rise.

- The organic matter in the MIS 1 floodplain sediments resembles mainly other Holocene deposits in the area and subordinately Yedoma material (MIS 3–2), which points to reworking.

- Fault line control on main discharge directions must be considered, especially for the southern edge, where the delta is bordering continental mountain ranges.

This study adds to existing models of the Lena River history and extends the environmental reconstruction further back in time. It sheds light on a Pleistocene river stream activity and a Holocene river delta formation where organic carbon is dynamically buried and reworked depending on stratigraphy. This is happening in an area that is sensitive to permafrost warming and undergoing longer open water seasons.

ACKNOWLEDGEMENTS

The financial and logistical support from AWI (Alfred Wegener Institute, Helmholtz Centre for Polar and Marine Research, Potsdam) is highly appreciated. We thank colleagues from AARI (Arctic and Antarctic Research Institute, St. Petersburg), IPGG (Trofimuk Institute for Petroleum Geology and Geophysics, Siberian Branch, Russian Academy of Sciences, Novosibirsk), and MPI-Y (Melnikov Permafrost Institute, Yakutsk) for making this drilling successful. ITU (Istanbul Technical University) supported the project through a BAP grant (ID: 42610 MAB-2021-42610). Loeka Jongejans, Mikhail Grigoriev, Dmitry Bolshiyarov, Paul Overduin, Antje Eulenburg, Mikaela Weiner, Justin Lindemann, Emin Çiftçi and Gültekin Topuz are thanked a lot, since they helped at various stages of sample processing. Comments of two reviewers (G. Fedorov and anonymous) on the first draft helped to improve the manuscript. The authors declare no conflict of interest with regard to this manuscript. We acknowledge support by the Open Access Publication Funds of the Alfred Wegener Institute, Helmholtz Centre for Polar and Marine Research. Open Access funding enabled and organized by Projekt DEAL.

DATA AVAILABILITY STATEMENT

The data that support the findings of this study are available from the PANGAEA database: Schwamborn *et al.* (2022).

REFERENCES

- ACIA (Arctic Climate Impact Assessment) (2004) *Impacts of a Warming Arctic: Arctic Climate Impact Assessment. Overview Report*, p. 140. Cambridge University Press, Cambridge.
- Aitchison, J. (1990) Relative variation diagrams for describing patterns of compositional variability. *Math. Geol.*, **22**, 487–511.
- Are, F. and Reimnitz, E. (2000) An overview of the Lena River Delta setting: geology, tectonics, geomorphology, and hydrology. *J. Coast. Res.*, **16**, 1083–1093.
- Avetisov, G.P. (1999) Geodynamics of the zone of continental continuation of Mid-Arctic earthquakes belt (Laptev Sea). *Phys. Earth Planet. In.*, **114**, 59–70.
- Bauch, H.A., Mueller-Lupp, T., Taldenkova, E., Spielhagen, R.F., Kassens, H., Grootes, P.M., Thiede, J., Heinemeier, J. and Petryashov, V.V. (2001) Chronology of the Holocene transgression at the North Siberian margin. *Global Planet. Change*, **31**, 125–139.
- Ben-Israel, M., Armon, M., ASTER Team and Matmon, A. (2022) Sediment residence times in large rivers quantified using a cosmogenic nuclides based transport model and implications for buffering of continental erosion signals. *J. Geophys. Res. Earth*, **127**, e2021JF006417.
- Biskaborn, B.K., Smith, S.L., Noetzli, J., Matthes, H., Vieira, G., Streletskiy, D.A., Schoeneich, P., Romanovsky, V.E., Lewkowicz, A.G., Abramov, A., Allard, M., Boike, J., Cable, W.L., Christiansen, H.H., Delaloye, R., Diekmann, B., Drozdov, D., Etzelmüller, B., Grosse, G., Guglielmin, M., Ingeman-Nielsen, T., Isaksen, K., Ishikawa, M., Johansson, M., Johannsson, H., Joo, A., Kaverin, D., Kholodov, A., Konstantinov, P., Kröger, T., Lambiel, C., Lanckman, J.-P., Luo, D., Malkova, G., Meiklejohn, I., Moskalenko, N., Oliva, M., Phillips, M., Ramos, M., Sannel, A.B.K., Sergeev, D., Seybold, C., Skryabin, P., Vasiliev, A., Wu, Q., Yoshikawa, K., Zheleznyak, M. and Lantuit, H. (2019) Permafrost is warming at a global scale. *Nat. Commun.*, **10**, 264.
- Blott, S.J. and Pye, K. (2001) Gradistat: a grain size distribution and statistics package for the analysis of unconsolidated sediments. *Earth Surf. Proc. Land.*, **26**, 1237–1248.
- Bolshiyarov, D., Makarov, A. and Savelieva, L. (2015) Lena River delta formation during the Holocene. *Biogeosciences*, **12**, 579–593.
- Bolshiyarov, D., Grigoriev, M., Maksimov, G., Straus, J., Schneider, W., Pushina, Z., Molodkov, A., Kuksa, K. and Petrov, A. (2020) Primary results of the 66-meters borehole drilling at Samoylov Island in the Lena River Delta. Proceedings of the Relief and Quaternary deposits of the Arctic, Subarctic and North-West Russia, Saint-Petersburg, Russia, 24–31. [in Russian with English abstract]
- Bonne, J.L., Meyer, H., Behrens, M., Boike, J., Kipfstuhl, S., Rabe, B., Schmidt, T., Schönicke, L., Steen-Larsen, H.C. and Werner, M. (2020) Moisture origin as a driver of temporal variabilities of the water vapour isotopic composition in the Lena River Delta, Siberia. *Atmos. Chem. Phys.*, **20**, 10493–10511.
- Bröder, L., Tesi, T., Salvadó, J.A., Semiletov, I.P., Dudarev, O.V. and Gustafsson, Ö. (2016) Fate of terrigenous organic matter across the Laptev Sea from the mouth of the Lena River to the deep sea of the Arctic interior. *Biogeosciences*, **13**, 5003–5019.
- Butler, R.F. and Butler, R.F. (1992) *Paleomagnetism: Magnetic Domains to Geologic Terranes* (Vol. 319). Blackwell Scientific Publications, Boston, MA.
- Craig, H. (1961) Isotopic variations in meteoric waters. *Science*, **133**, 1702–1703.
- Croudace, I.W., Rindby, A. and Rothwell, R.G. (2006) ITRAX: description and evaluation of a new multi-function X-ray core scanner. *Geol. Soc. Lond. Spec. Publ.*, **267**, 51–63.
- Dansgaard, W. (1964) Stable isotopes in precipitation. *Tellus*, **16**, 436–468.
- Davidson, E.A. and Janssens, I.A. (2006) Temperature sensitivity of soil carbon decomposition and feedbacks to climate change. *Nature*, **440**, 165–173.
- Drachev, S.S. (2016) Fold belts and sedimentary basins of the Eurasian Arctic. *Ark. Dent.*, **2**, 1–30.
- Dyke, L.D. (2000) Shoreline permafrost along the Mackenzie River. In: *The Physical Environment of the Mackenzie Valley, Northwest Territories: A Base Line for the Assessment of Environmental Change* (Eds Dyke, L.D. and Brooks, G.R.), Geological Survey of Canada, Bulletin, **547**, 143–151.
- Fedorova, I., Chetverova, A., Bolshiyarov, D., Makarov, A., Boike, J., Heim, B., Morgenstern, A., Overduin, P.P., Wegner, C., Kashina, V., Eulenburg, A., Dobrotina, E. and Sidorina, I. (2015) Lena Delta hydrology and geochemistry: long-term hydrological data and recent field observations. *Biogeosciences*, **12**, 345–363.
- Fofonova, V., Zhilyaev, I., Kraineva, M., Iakshina, D., Tananaev, N., Volkova, N., Sander, L., Papenmeier, S., Michaelis, R. and Wiltshire, K.H. (2018) Features of the water temperature long-term observations on the Lena River at basin outlet. *Polarforschung*, **87**, 135–150.
- Franke, D. and Hinz, K. (2009) Geology of the Shelves surrounding the New Siberian Islands, Russian Arctic. *Stephan Mueller Special Publication Series*, **4**, 35–44.
- French, H. and Shur, Y. (2010) The principles of cryostratigraphy. *Earth-Sci. Rev.*, **101**, 190–206.
- Fritz, M., Wetterich, S., Meyer, H., Schirrmeister, L., Lantuit, H. and Pollard, W.H. (2011) Origin and characteristics of massive ground ice on Herschel Island (western Canadian Arctic) as revealed by stable water isotope and Hydrochemical signatures. *Permafrost Periglac. Process.*, **22**, 26–38.
- Fuchs, M., Nitzte, I., Strauss, J., Gunther, F., Wetterich, S., Kizyakov, A., Fritz, M., Opel, T., Grigoriev, M.N., Maksimov, G.T. and Grosse, G. (2020) Rapid Fluvio-Thermal Erosion of a Yedoma Permafrost Cliff in the Lena River Delta. *Front. Earth Sci.*, **8**, 336.
- Fujita, K., Koz'min, B.M., Mackey, K.G., Riegel, S.A., McLean, M.S. and Imaev, V.S. (2009) Seismotectonics of the Chersky Seismic Belt, eastern Sakha Republic (Yakutia) and Magadan District, Russia. *Stephan Mueller Special Publication Series*, **4**, 117–145.
- Gingele, F.X., De Deckker, P. and Hillenbrand, C.D. (2001) Clay mineral distribution in surface sediments between Indonesia and NW Australia – source and transport by ocean currents. *Mar. Geol.*, **179**, 135–146.
- Grigoriev, M.N. (1993) *Criomorphogenesis in the Lena Delta*, p. 176. Permafrost Institute Press, Yakutsk. [in Russian].
- Hammer, Ø., Harper, D.A. and Ryan, P.D. (2001) PAST: paleontological statistics software package for education and data analysis. *Palaeontol. Electron.*, **4**, 9.
- Harrison, J. C., St-Onge, M. R., Petrov, O.V., Strelnikov, S. I., Lopatin, B. G., Wilson, F. H., Tella, S., Paul, D., Lynds,

- T., Shokalsky, S. P., Hults, C. K., Bergman, S., Jepsen, H. F. and Solli, A. (2011) Geological map of the Arctic: Geological Survey of Canada Map 2159A. <https://doi.org/10.4095/287868> via <https://macrostrat.org/> (access: Feb-2022)
- Haugk, C., Jongejans, L.L., Mangelsdorf, K., Fuchs, M., Ogneva, O., Palmtag, J., Mollenhauer, G., Mann, P.J., Overduin, P.P., Grosse, G., Sanders, T., Tuerena, R.E., Schirrmeyer, L., Wetterich, S., Kizyakov, A., Karger, C. and Strauss, J. (2022) Organic matter characteristics of a rapidly eroding permafrost cliff in NE Siberia (Lena Delta, Laptev Sea region). *Biogeosciences*, **2022**, 2079–2094. <https://doi.org/10.5194/bg-2021-331>.
- Heimann, M. and Reichstein, M. (2008) Terrestrial ecosystem carbon dynamics and climate feedbacks. *Nature*, **451**, 289–292.
- Holmes, M.L. and Creager, J.S. (1974) Holocene history of the Laptev continental shelf. In: *Marine Geology and Oceanography* (Ed Herman, Y.), pp. 211–229. Springer, Berlin.
- Jongejans, L.L., Assmann, V., Boike, J., Bolshiyarov, D., Bornemann, N., Grigoriev, B., Grigoriev, M.N., Kartoziia, A., Maksimov, G., Ostredin, S., Ostredin, S., Schneider, W., Schreiber, P., Tsigizov, L. and Strauss, J. (2019) Samoylov Deep Drilling Spring Campaign 2018. In: *Russian-German Cooperation: Expeditions to Siberia in 2018* (Eds Kruse, S., Bolshiyarov, D., Grigoriev, M.N., Morgenstern, A., Pestryakova, L., Tsigizov, L. and Udke, A.), *Berichte zur Polar- und Meeresforschung = Reports on polar and marine research, Bremerhaven, Alfred Wegener Institute Helmholtz Centre for Polar and Marine Research, Bremerhaven, Germany*, **734**, 11–23.
- Jongejans, L.L., Liebner, S., Knoblauch, C., Mangelsdorf, K., Ulrich, M., Grosse, G., Tanski, G., Fedorov, A.N., Konstantinov, P.Y., Windirsch, T., Wiedmann, J. and Strauss, J. (2021) Greenhouse gas production and lipid biomarker distribution in Yedoma and Alas thermokarst lake sediments in Eastern Siberia. *Glob. Chang. Biol.*, **27**, 2822–2839.
- Juhls, B., Stedmon, C.A., Morgenstern, A., Meyer, H., Hölemann, J., Heim, B., Povazhnyi, V. and Overduin, P.P. (2020) Identifying drivers of seasonality in Lena River biogeochemistry and dissolved organic matter fluxes. *Front. Environ. Sci.*, **8**, 53.
- Kienast, F., Tarasov, P., Schirrmeyer, L., Grosse, G. and Andreev, A.A. (2008) Continental climate in the East Siberian Arctic during the last interglacial: implications from palaeobotanical records. *Global Planet. Change*, **60**, 535–562.
- Kienast, F., Wetterich, S., Kuzmina, S., Schirrmeyer, L., Andreev, A., Tarasov, P., Nazarova, L., Kossler, A., Frolova, A. and Kunitsky, V.V. (2011) Paleontological records indicate the occurrence of open woodlands in a dry inland climate at the present-day Arctic coast in western Beringia during the last interglacial. *Quatern. Sci. Rev.*, **30**, 2134–2159.
- Kleiber, H.P. and Niessen, F. (1999) Late Pleistocene Paleoriver channels on the Laptev Sea shelf implications from sub-bottom profiling. In: *Land-ocean Systems in the Siberian Arctic: Dynamics and History* (Eds Kassens, H., Bauch, H., Dmitrenko, I., Eicken, H., Hubberten, H.-W., Melles, M., Thiede, J. and Timokhov, L.), pp. 657–665. Springer, Berlin.
- Kleiber, P. and Niessen, F. (2000) Variations of continental discharge pattern in space and time: implications from the Laptev Sea continental margin, Arctic Siberia. *Int. J. Earth Sci.*, **89**, 605–616.
- Klemann, V., Heim, B., Bauch, H.A., Wetterich, S. and Opel, T. (2015) Sea-level evolution of the Laptev Sea and the East Siberian Sea since the last glacial maximum. *Ark. Dent.*, **1**, 1–8.
- Korotaev, V.N. (2011) The holocene history of the River Deltas Along the Arctic Coast of Siberia. *Geogr. Nat. Resour.*, **32**, 213–219.
- Kurita, N., Numaguti, A., Sugimoto, A., Ichiyanagi, K. and Yoshida, N. (2003) Relationship between the variation of isotopic ratios and the source of summer precipitation in eastern Siberia. *J. Geophys. Res. Atmos.*, **108**, D11.
- Lacelle, D. (2011) On the $\delta^{18}\text{O}$, δD and D-excess relations in meteoric precipitation and during equilibrium freezing: theoretical approach and field examples. *Permafrost. Periglac. Process.*, **22**, 13–25.
- Lacelle, D., Bjornson, J., Lauriol, B., Clark, I.D. and Troutet, Y. (2004) Segregated-intrusive ice of subglacial meltwater origin in retrogressive thaw flow headwalls, Richardson Mountains, N.W.T., Canada. *Quatern. Sci. Rev.*, **23**, 681–696.
- Lecoanet, H., Lévêque, F. and Segura, S. (1999) Magnetic susceptibility in environmental applications: comparison of field probes. *Phys. Earth Planet. In.*, **115**, 191–204.
- Lukina, N. V., Patyk-Kara, N. G. and Sokolov, S. Y. (2003) Russian Arctic Seas – Neotectonic Structures and Active Faults 3-4. Ed. Trifonov, V. G. In: *Atlas: Geology and Mineral Resources of the Russian Shelf Areas* (Ed. Alekseev, M.N.). Moscow: Nauchn. Mir / GIN-RAS.
- Mange, M.A. and Maurer, H. (2012) *Heavy Minerals in Colour*, p. 147. Chapman and Hall, London.
- Martens, J., Wild, B., Muschiello, F., O'Regan, M., Jakobsson, M., Semiletov, I., Dudarev, O.V. and Gustafsson, Ö. (2020) Remobilization of dormant carbon from Siberian-Arctic permafrost during three past warming events. *Sci. Adv.*, **6**, eabb6546.
- Meyer, H., Schönicke, L., Wand, U., Hubberten, H.W. and Friedrichsen, H. (2000) Isotope studies of hydrogen and oxygen in ground ice-experiences with the equilibration technique. *Isotopes Environ. Health Stud.*, **36**, 133–149.
- Meyer, H., Derevyagin, A.Y., Siegert, C. and Hubberten, H.W. (2002) Paleoclimate studies on Bykovsky Peninsula, North Siberia-hydrogen and oxygen isotopes in ground ice. *Polarforschung*, **70**, 37–51.
- Meyer, H., Schirrmeyer, L., Yoshikawa, K., Opel, T., Wetterich, S., Hubberten, H.-W. and Brown, J. (2010) Permafrost evidence for severe winter cooling during the Younger Dryas in northern Alaska. *Geophys. Res. Lett.*, **37**, L03501.
- Meyers, P.A. and Teranes, J.L. (2001) Sediment organic matter. In: *Tracking Environmental Change Using Lake Sediments, Vol. 2: Physical and Geochemical Methods* (Eds Last, W.M. and Smol, J.P.), pp. 239–269. Kluwer Academic Publishers, Dordrecht, The Netherlands.
- Mock, J., Bartlein, P.J. and Anderson, P.A. (1998) Atmospheric circulation patterns and spatial climatic variations in Beringia. *Int. J. Climatol.*, **10**, 1085–1104.
- Mollenhauer, G., Grotheer, H., Gentz, T., Bonk, E. and Hefter, J.H. (2021) Standard operation procedures and performance of the MICADAS radiocarbon laboratory at Alfred Wegener Institute (AWI), Germany. *Nucl. Instrum. Methods Phys. Res. B*, **496**, 45–51.
- Molodkov, A. (2020) The Late Pleistocene palaeoenvironmental evolution in Northern Eurasia

- through the prism of the mollusc shell-based ESR dating evidence. *Quat. Int.*, **556**, 180–197.
- Murton, J.B., Goszlar, T., Edwards, M.E., Bateman, M.D., Danilov, P.P., Savinov, G.N., Gubin, S.V., Ghaleb, B., Haile, J., Kanevskiy, M., Lozhkin, A.V., Lupachev, A.V., Murton, D.K., Shur, Y., Tikhonov, A., Vasil'chuk, A.C., Vasil'chuk, Y.K. and Wolfe, S.A.** (2015) Palaeoenvironmental interpretation of Yedoma Silt (ice complex) deposition as cold-climate loess, Duvanny Yar, Northeast Siberia. *Permafrost Periglac. Process.*, **26**, 208–288.
- Natali, C., Bianchini, G. and Carlino, P.** (2020) Thermal stability of soil carbon pools: inferences on soil nature and evolution. *Thermochim. Acta*, **683**, 178478.
- Pavlova, E.Y. and Dorozhkina, M.V.** (2000) The Holocene alluvial delta relief complex and hydrological regime of the Lena River Delta. *Polarforschung*, **70**, 89–100.
- Peregovich, B., Hoops, E. and Rachold, V.** (1999) Sediment transport to the Laptev Sea (Siberian Arctic) during the Holocene – evidence from the heavy mineral composition of fluvial and marine sediments. *Boreas*, **28**, 205–214.
- Piliouras, A. and Rowland, J.C.** (2020) Arctic river delta morphologic variability and implications for riverine fluxes to the coast. *J. Geophys. Res. Earth*, **125**, e2019JF005250.
- Porter, T.J. and Opel, T.** (2020) Recent advances in paleoclimatological studies of Arctic wedge- and pore-ice stable-water isotope records. *Permafrost Periglac. Process.*, **19**, 170088.
- Potter, P.E., Huh, Y. and Edmond, J.M.** (2001) Deep-freeze petrology of Lena River sand, Siberia. *Geology*, **29**, 999–1002.
- Prokopenko, A., Williams, D.F., Kavel, P. and Karabanov, E.** (1993) The organic indexes in the surface sediments of Lake Baikal water system and the processes controlling their variation. *IPPCC Newslett.*, **7**, 49–55.
- Prokopiev, A.V., Toro, J., Hourigan, J.K., Bakharev, A.G. and Miller, E.L.** (2009) Middle Paleozoic-Mesozoic boundary of the North Asian craton and the Okhotsk terrane: new geochemical and geochronological data and their geodynamic interpretation. *Stephan Mueller Special Publication Series*, **4**, 71–84.
- Puminov, A.P.** (1960) On the history of the river valleys of the lower sections of the Lena and Olenek Rivers. *Tr. NIIGA*, **114**, 163–172 [in Russian].
- Rekant, P., Bauch, H.A., Schwenk, T., Portnov, A., Gusev, E., Spiess, V., Cherkashov, G. and Kassens, H.** (2015) Evolution of subsea permafrost landscapes in Arctic Siberia since the Late Pleistocene: a synoptic insight from acoustic data of the Laptev Sea. *Ark. Dent.*, **1**, 1–15.
- Schirrmeister, L., Siegert, C., Kuznetsova, T., Kuzmina, S., Andreev, A., Kienast, F., Meyer, H. and Bobrov, A.** (2002) Paleoenvironmental and paleoclimatic records from permafrost deposits in the Arctic region of Northern Siberia. *Quat. Int.*, **89**, 97–118.
- Schirrmeister, L., Kunitsky, V.V., Grosse, G., Schwamborn, G., Andreev, A.A., Meyer, H., Kuznetsova, T., Bobrov, A. and Oezen, D.** (2003) Late Quaternary history of the accumulation plain north of the Chekanovsky Ridge (Lena Delta, Russia) - a multidisciplinary approach. *Polar Geogr.*, **27**, 277–319.
- Schirrmeister, L., Grosse, G., Kunitsky, V., Magens, D., Meyer, H., Derevyagin, A.Y., Kuznetsova, T., Andreev, A., Babiy, O., Kienast, F., Grigoriev, M., Overduin, P.P. and Preusser, F.** (2008) Periglacial landscape evolution and environmental changes of Arctic lowland areas for the last 60,000 years (Western Laptev Sea coast, Cape Mamontov Klyk). *Polar Res.*, **27**, 249–272.
- Schirrmeister, L., Grosse, G., Schnelle, M., Fuchs, M., Krbetschek, M., Ulrich, M., Kunitsky, V., Grigoriev, M., Andreev, A., Kienast, F., Meyer, H., Klimova, I., Babiy, O., Bobrov, A., Wetterich, S. and Schwamborn, G.** (2011) Late Quaternary paleoenvironmental records from the western Lena Delta, Arctic Siberia. *Palaeogeogr. Palaeoclimatol. Palaeoecol.*, **299**, 175–196.
- Schirrmeister, L., Froese, D., Tumskey, V., Grosse, G. and Wetterich, S.** (2013) Yedoma: Late Pleistocene ice-rich syngenetic permafrost of Beringia. In: *Encyclopedia of Quaternary Science* (Eds Elias, S.A. and Mock, C.J.), 2nd edn, Vol. 2, pp. 542–552. Elsevier, Amsterdam.
- Schirrmeister, L., Dietze, E., Matthes, H., Grosse, G., Strauss, J., Laboor, S., Ulrich, M., Kienast, F. and Wetterich, S.** (2020) The genesis of Yedoma Ice Complex permafrost – grain-size endmember modeling analysis from Siberia and Alaska. *E&G Quatern. Sci. J.*, **69**, 33–53.
- Schirrmeister, L., Wetterich, S., Schwamborn, G., Matthes, H., Grosse, G., Klimova, I., Kunitsky, V.V. and Siegert, C.** (2022) Heavy and light mineral associations of late Quaternary permafrost deposits in Northeastern Siberia. *Front. Earth Sci.*, **10**, 741932.
- Schuur, E.A., Bockheim, J., Canadell, J.G., Euskirchen, E., Field, C.B., Goryachkin, S.V., Hagemann, S., Kuhry, P., Laflour, P.M., Lee, H., Mazhitova, G., Nelson, F.E., Rinke, A., Romanovsky, V.E., Shiklomanov, N., Tarnocai, C., Venevsky, S., Vogel, J.G. and Zimov, S.A.** (2008) Vulnerability of permafrost carbon to climate change: Implications for the global carbon cycle. *Bioscience*, **58**, 701–714.
- Schwamborn, G., Andreev, A., Rachold, V., Hubberten, H.W., Grigoriev, M.N., Tumskey, V., Pavlova, E.Y. and Dorozhkina, M.V.** (2000) Evolution of Lake Nikolay, Arga Island, Western Lena River delta, during late Pleistocene and Holocene time. *Polarforschung*, **70**, 69–82.
- Schwamborn, G., Rachold, V. and Grigoriev, M.N.** (2002) Late quaternary sedimentation history of the Lena Delta. *Quat. Int.*, **89**, 119–134.
- Schwamborn, G., Meyer, H., Schirrmeister, L. and Fedorov, G.** (2014) Past freeze and thaw cycling in the margin of the El'gygytgyn crater deduced from a 141 m long permafrost record. *Climate Past*, **10**, 1109–1123.
- Schwamborn, G., Schirrmeister, L., Mohammadi, A., Meyer, H., Kartoziia, A., Maggioni, F. and Strauss, J.** (2022) SAM18-01 Samoylov permafrost drilling, Lena Delta, NE Siberia. *Pangaea*. <https://doi.org/10.1594/PANGAEA.945355>.
- Siegert, C., Schirrmeister, L. and Babiy, O.** (2002) The sedimentological, mineralogical and geochemical composition of Late Pleistocene deposits from the Ice Complex on the Bykovsky Peninsula Northern Siberia. *Polarforschung*, **70**, 3–11.
- Spielhagen, R.F., Erlenkeuser, H. and Siegert, C.** (2005) History of freshwater runoff across the Laptev Sea (Arctic) during the last deglaciation. *Global Planet. Change*, **48**, 187–207.
- Spratt, R.M. and Lisiecki, L.E.** (2016) A Late Pleistocene sea level stack. *Climate Past*, **12**, 1079–1092.
- Stauch, G. and Lehmkuhl, F.** (2010) Quaternary glaciations in the Verkhoyansk Mountains, northeast Siberia. *Quat. Res.*, **74**, 145–155.

- Strauss, J., Schirrmeister, L., Mangelsdorf, K., Eichhorn, L., Wetterich, S. and Herzschuh, U. (2015) Organic-matter quality of deep permafrost carbon – a study from Arctic Siberia. *Biogeosciences*, **12**, 2227–2245.
- Strauss, J., Schirrmeister, L., Grosse, G., Fortier, D., Hugelius, G., Knoblauch, C., Romanovsky, V., Schädel, C., Schneider von Deimling, T., Schuur, E.A.G., Shmelev, D., Ulrich, M. and Veremeeva, A. (2017) Deep Yedoma permafrost: a synthesis of depositional characteristics and carbon vulnerability. *Earth-Sci. Rev.*, **172**, 75–86.
- Strauss, J., Abbott, B., Hugelius, G., Schuur, E.A.G., Treat, C., Fuchs, M., Schädel, C., Ulrich, M., Turetsky, M.R., Keuschnig, M., Biasi, C., Yang, Y. and Grosse, G. (2021a) Permafrost. In: *Recarbonizing Global Soils – A Technical Manual of Recommended Management Practices* (Ed. Food and Agriculture Organization of the United Nations (FAO), a. I. T. P. o. S. I.), pp. 127–147. Food and Agriculture Organization of the United Nations, Rome, Italy.
- Strauss, J., Laboor, S., Schirrmeister, L., Fedorov, A.N., Fortier, D., Froese, D., Fuchs, M., Günther, F., Grigoriev, M., Harden, J., Hugelius, G., Kanevskiy, M., Kholodov, A., Kunitsky, V., Kraev, G., Lozhkin, A., Rivkina, E., Shur, Y., Siegert, C., Spektor, V., Streletskaya, I., Ulrich, M., Vartanyan, S., Veremeeva, A., Walter Anthony, K., Zimov, N. and Grosse, G. (2021b) Circum-Arctic Map of the Yedoma Permafrost Domain. *Front. Earth Sci.*, **9**, 758360.
- Stuiver, M. and Reimer, P.J. (1993) Extended ^{14}C data base and revised CALIB 3.0 ^{14}C age calibration program. *Radiocarbon*, **35**, 215–230.
- Turetsky, M.R., Abbott, B.W., Jones, M.C., Anthony, K.W., Olefeldt, D., Schuur, E.A., Schuur, E.A.G., Koven, C., McGuire, A.D., Grosse, G., Kuhry, P., Hugelius, G., Lawrence, D.M., Gibson, C. and Sannel, A.B.K. (2019) Permafrost collapse is accelerating carbon release. *Nature*, **569**, 32–34.
- Vonk, J.E., Dickens, A.F., Giosan, L., Hussain, Z.A., Kim, B., Zipper, S.C., Holmes, R.M., Montlucon, D.B., Galy, V. and Eglinton, T.I. (2016) Arctic Deltaic Lake sediments as recorders of fluvial organic matter deposition. *Front. Earth Sci.*, **4**, 77.
- Wetterich, S., Kuzmina, S., Andreev, A.A., Kienast, F., Meyer, H., Schirrmeister, L., Kuznetsova, T. and Sierralta, M. (2008) Palaeoenvironmental dynamics inferred from late Quaternary permafrost deposits on Kurungnakh Island, Lena Delta, Northeast Siberia, Russia. *Quatern. Sci. Rev.*, **27**, 1523–1540.
- Wetterich, S., Schirrmeister, L., Andreev, A.A., Pudenz, M., Plessen, B., Meyer, H. and Kunitsky, V.V. (2009) Eemian and Late Glacial/Holocene palaeoenvironmental records from permafrost sequences at the Dmitry Laptev Strait (NE Siberia, Russia). *Palaeogeogr. Palaeoclimatol. Palaeoecol.*, **279**, 73–95.
- Wetterich, S., Rudaya, N., Kuznetsov, V., Maksimov, F., Opel, T., Meyer, H., Günther, F., Bobrov, A., Raschke, E., Zimmermann, H., Strauss, J., Starikova, A., Fuchs, M.C. and Schirrmeister, L. (2019) Ice complex formation on Bol'shoy Lyakhovsky Island (New Siberian Archipelago, East Siberian Arctic) since about 200 ka. *Quatern. Res.*, **92**, 530–548.
- Wetterich, S., Kizyakov, A., Fritz, M., Wolter, J., Mollenhauer, G., Meyer, H., Fuchs, M., Aksenov, A., Matthes, H., Schirrmeister, L. and Opel, T. (2020) The cryostratigraphy of the Yedoma cliff of Sobo-Sise Island (Lena delta) reveals permafrost dynamics in the central Laptev Sea coastal region during the last 52 kyr. *Cryosphere*, **14**, 4525–4551.
- Wetterich, S., Rudaya, N., Nazarova, L., Syrykh, L., Pavlova, M., Palagushkina, O., Kizyakov, A., Wolter, J., Kuznetsova, T., Aksenov, A., Stoof-Leichsenring, K.R., Schirrmeister, L. and Fritz, M. (2021) Paleo-ecology of the Yedoma Ice Complex on Sobo-Sise Island (Eastern Lena Delta, Siberian Arctic). *Front. Earth Sci.*, **9**, 681511.
- Whitehouse, P.L., Allen, M.A. and Milne, G.A. (2007) Glacial isostatic adjustment as a control on coastal processes: An example from the Siberian Arctic. *Geology*, **35**, 747–750.
- Winterfeld, M., Schirrmeister, L., Grigoriev, M., Kunitsky, V.V., Andreev, A., Murray, A. and Overduin, P.P. (2011) Coastal permafrost landscape development since the Late Pleistocene in the western Laptev Sea, Siberia. *Boreas*, **40**, 697–713.
- Winterfeld, M., Goñi, M.A., Just, J., Hefter, J. and Mollenhauer, G. (2015) Characterization of particulate organic matter in the Lena River delta and adjacent nearshore zone, NE Siberia–Part 2: Lignin-derived phenol compositions. *Biogeosciences*, **12**, 2261–2283.
- Zibulski, R., Wesener, F., Wilkes, H., Plessen, B., Pestryakova, L.A. and Herzschuh, U. (2017) C/N ratio, stable isotope ($\delta^{13}\text{C}$, $\delta^{15}\text{N}$), and n-alkane patterns of brown mosses along hydrological gradients of low-centred polygons of the Siberian Arctic. *Biogeosciences*, **14**, 1617–1630.
- Zimov, S.A., Schuur, E.A. and Chapin, F.S., III (2006) Permafrost and the global carbon budget. *Science*, **312**, 1612–1613.

Manuscript received 23 March 2022; revision accepted 20 August 2022

Supporting Information

Additional information may be found in the online version of this article:

Figure S1. Microphotographs of selected samples from fraction 2–3.15 mm (crossed polarized light): (A) sample from 64.00–63.85 m depth; (B) sample from 57.60–57.50 m depth; (C) sample from 54.85–54.40 m depth; (D) sample from 50.77–50.57 m depth; (E) sample from 47.47–46.90 m depth; (F) sample from 27.44–27.17 m depth. Co, conglomerate; Sa, sandstone; Si, siltstone; Li, limestone; Gr, granite; OGr, orbicular granite; VL, volcanic lithic; PVL, porphyry volcanic lithic; ML, metamorphic lithic; LML, low-grade metamorphic lithic; HML, high-grade metamorphic lithic; PQ, polycrystalline quartz.